QUARTERLY JOURNAL
OF THE
ROYAL METEOROLOGICAL SOCIETY

Vol. 125 JANUARY 1999 Part B No. 554

Q. J. R. Meteorol. Soc. (1999), **125**, pp. 391–423

An intercomparison of radiatively driven entrainment and turbulence in a smoke cloud, as simulated by different numerical models

By C. S. BRETHERTON[1]*, M. K. MACVEAN[2], P. BECHTOLD[3], A. CHLOND[4], W. R. COTTON[5], J. CUXART[6], H. CUIJPERS[7], M. KHAIROUTDINOV[8], B. KOSOVIC[9], D. LEWELLEN[10], C.-H. MOENG[11], P. SIEBESMA[7], B. STEVENS[11], D. E. STEVENS[12], I. SYKES[13] and M. C. WYANT[1]

[1]*University of Washington, USA*
[2]*Meteorological Office, UK*
[3]*Observatoire Midi-Pyrénées, France*
[4]*Max-Planck Institut für Meteorologie, Germany*
[5]*Colorado State University, USA*
[6]*Instituto Nacional de Meteorologia, Spain*
[7]*Institute for Marine and Atmospheric Research, The Netherlands*
[8]*University of Oklahoma, USA*
[9]*University of Colorado, USA*
[10]*West Virginia University, USA*
[11]*National Center for Atmospheric Research, USA*
[12]*Lawrence Berkeley Laboratory, USA*
[13]*Titan Research and Technology, USA*

(Received 1 April 1997; revised 15 December 1997)

SUMMARY

As part of a programme of intercomparison of eddy-resolving and one-dimensional (1-D) boundary-layer models, a convective boundary-layer filled with radiatively active 'smoke' was simulated. The programme is sponsored by the Global Energy and Water Experiment Cloud Systems Study. Cloud-top-cooling rates were chosen to be comparable with those observed in marine stratocumulus, while avoiding evaporative feedbacks on entrainment and turbulence that are also important in liquid-water clouds. The radiative-cooling rate had a specified dependence on the smoke profile, so that differences between simulations could only be a result of different numerical representations of fluid motion and subgrid-scale turbulence. At a workshop in De Bilt, The Netherlands in August 1995, results from numerous groups around the world were compared with each other and with a previously investigated laboratory analogue to the smoke cloud.

The intercomparison results show that models must be run with higher vertical resolution in the inversion than is customary at present, in order to accurately simulate the entrainment rate into cloud-topped boundary-layers under strong inversions. In three-dimensional (3-D) models using a vertical grid spacing of 5–12.5 m, sufficient to resolve the horizontal variability of inversion height, entrainment rates were 10–50% larger than the range consistent with the laboratory experiments. With a larger vertical grid spacing of 25 m, 1-D, 2-D and 3-D models all overestimated the entrainment rate by more than 50%. 3-D models with monotone advection-schemes overestimated entrainment slightly more than those with non-monotone schemes, at least when 25 m vertical grid-spacing was used. However, results from non-monotone schemes had several undesirable features associated with the generation of undershoots and overshoots, most notably spurious turbulent mixing above the smoke layer. The 1-D models tended to underestimate turbulent kinetic energy (TKE) but performed reasonably well given their simplicity. 2-D models produced too much entrainment and considerably overestimated TKE, compared with 3-D models with the same numerical formulation.

Based on a simple scaling-argument, we propose that the minimum vertical grid-spacing required to obtain an accurate entrainment-rate is of the order of the horizontal fluctuations in inversion height, which is proportional to the layer-averaged TKE and inversely proportional to the inversion strength.

KEYWORDS: Entrainment Large-eddy simulation Stratocumulus

* Corresponding author: University of Washington, Department of Atmospheric Sciences, Box 351640, Seattle, WA 98195-1640, USA.

1. Introduction

The factors affecting entrainment at the top of the atmospheric boundary-layer are many and complex, particularly when cloud is present. The parametrization of entrainment is a major area of uncertainty in current models used for numerical weather prediction and climate studies (Randall *et al.* 1985; Del Genio *et al.* 1996). Direct measurements of entrainment into cloud-topped boundary-layers are difficult, have measurement uncertainties of 50% or more, and only a few reliable studies are available (e.g., Nicholls and Turton 1986; Kawa and Pearson 1989; Bretherton *et al.* 1995; de Roode and Duynkerke 1997). Hence, it is attractive to develop parametrizations based on numerical models which resolve cloud-scale motions or from laboratory experiments, as a proxy for atmospheric data. One can have confidence in parametrizations developed in this way only if there is reasonable agreement between results from different models, laboratory experiments and the limited atmospheric data available. In response to these requirements, the Boundary Layer Cloud working group of the Global Energy and Water Experiment Cloud Systems Study (GCSS) (see GEWEX Cloud System Science Team (1993) for an overview) has an ongoing programme of intercomparison of cloud-resolving models, focused, where possible, on cases where some independent data are available.

The first such intercomparison took place in August 1994 and involved large-eddy simulations (LESs) of an idealized stratocumulus case under a strong marine inversion, loosely based on observations from the First International Satellite Cloud Climatology Project Regional Experiment (FIRE) marine stratocumulus experiment in 1987. The case involved a solid cloud-deck with a high degree of horizontal homogeneity, no drizzle, no solar radiation, little wind-shear and weak surface-heating. The results from the various models, discussed by Moeng *et al.* (1996), showed broad agreement in many aspects of the overall cloud-structure and in the vertical distributions of many turbulence statistics, but an alarming scatter (6–21 mm s^{-1}) in the entrainment velocity. This range of model entrainment-velocities is broadly consistent with typical values observed in stratocumulus of around 5 mm s^{-1}. However, entrainment rates were not measured for the specific FIRE case. Even if they had been, the test case was too idealized for conclusive observational comparisons.

The different models used a wide variety of numerical schemes for advection and for the parametrization of subgrid-scale turbulence. Such basic differences between models may account for some of the variation in the entrainment rates. However, other model differences may also contribute substantially to the scatter. The major sources of turbulence in these simulations were long-wave radiative-cooling and evaporative cooling. Both processes occur primarily near the cloud top and are strongly dependent on the liquid-water content there. During the analysis, it became apparent that there were significant differences in the initial liquid-water profiles in the models (up to 25%), caused by the differing algorithms used to diagnose this from the specified profiles of total-water mixing-ratio and potential temperature. Such differences can directly affect the intensity of the turbulence and may have accounted for some of the variation in the entrainment velocities. Significant differences between the long-wave radiation schemes and, in particular, the downwelling long-wave radiation at the cloud top in different models may also have contributed to this scatter.

The consensus at the workshop was that, in order to improve the models, it was necessary to separate the scatter caused by the different numerical representations of fluid motion and subgrid-scale turbulence from the scatter caused by the model differences in radiation and microphysics. It was agreed that a useful next step would be to consider a situation in which radiative cooling was the only source of turbulence and all the compli-

cations associated with liquid water were circumvented. In this analogue, first proposed by Lilly (1968), the turbulent layer is filled with an optically thick layer of radiatively active smoke (a 'smoke cloud'), resulting in concentrated radiative cooling just below the entrainment interface, which in turn drives convection, as in a marine stratocumulus cloud-topped boundary-layer. An intercomparison of model results for a 'smoke cloud' below a strong inversion, discussed at a workshop in De Bilt, The Netherlands, in August 1995, forms the basis for the present paper.

A second motivation for studying the smoke-cloud case is that it is directly comparable with laboratory studies. McEwan and Paltridge (1976) and Sayler and Breidenthal (1997, hereafter SB97) investigated an inverted analogue to the smoke cloud. They used a tank containing a layer of blue fluid overlying a denser layer of yellow fluid. The tank was illuminated from below by yellow light. Selective absorption of the light in the blue fluid just above the interface resulted in convection in the upper layer. The entrainment rate was measured as the rate of change of the mean height of the interface. By controlling the density difference between the fluids and the intensity of the illumination, SB97 found scaling relations for the entrainment rate of the yellow fluid by the blue fluid of the form

$$w_e/U = A/Ri, \tag{1}$$

where $A = 0.2$ is a nondimensional constant, and U is a convective velocity scale. For buoyancy-driven flows, U is derived from the vertical integral of buoyancy flux (see section 2 for a precise definition). The bulk interfacial Richardson number is

$$Ri = z_i \Delta b / U^2, \tag{2}$$

where z_i is the thickness of the convecting layer and Δb is the 'buoyancy jump', or the density jump across the inversion scaled into a buoyant acceleration. The earlier measurements of McEwan and Paltridge (1976) spanned a much narrower range of Richardson numbers insufficient to indicate this scaling clearly, but are consistent with SB97's measurements in the range of overlap.

The analogy with the smoke cloud is not exact, since the working fluid in the laboratory experiments, water, has a Prandtl number Pr (ratio of kinematic viscosity to heat diffusivity) of 7, while air has $Pr = 0.7$. SB97 also performed experiments in which the initial stratification between the fluids was produced not with heat but with sugar (which has a diffusivity only 0.05% as large as heat). They found the same scaling-relation, but with A reduced by a factor of three. This suggests that the entrainment rate may roughly scale as $Pr^{-0.2}$, which would imply that for air, A would be 0.3–0.4 . Also, the convection in laboratory experiments has a Reynolds number Re of a few hundred, while an atmospheric boundary layer has $Re \approx 10^8$. Whereas the large eddies in the laboratory experiment are fully turbulent, the entrainment processes, which occur in the narrow interfacial zone, are not, especially for larger values of Ri. SB97 argue from experience with related experiments that this should not greatly affect the entrainment rate, especially for fluids like air with Pr of the order of one.

The third important motivation for the smoke-cloud intercomparison is the A-dilemma'—the puzzling fact that the laboratory experiments predict an entrainment efficiency A up to 10 times smaller than available observations in stratocumulus-capped boundary-layers would suggest (Nicholls and Turton 1986). A few possible explanations for this large difference can be examined. The first is that the laboratory experiments lead to incorrect predictions of entrainment in an atmospheric smoke-layer radiatively driven from its top. A second is that mixing-induced evaporation at the top of liquid-water clouds greatly enhances A. A third is that the inversion structure is more complex in the

atmosphere than in a smoke cloud (for instance, because of wind shear in the inversion or above-inversion radiative cooling). In particular, Nieuwstadt and Businger (1984) and others have estimated that in a nocturnal stratocumulus-capped boundary-layer, up to 10% as much cooling occurred in the lowest 100 m above the turbulent layer as within the cloud. This results in a stable layer just above the inversion which may alter the entrainment dynamics and hence change the inferred A. Since the inversion interface is irregular, it can also sometimes be difficult to separate the inversion jump and the strongly stable layer above, resulting in possible overestimation of the inversion jumps and hence of A. A fourth possible explanation for the large A in stratocumulus is that the vertical structure of the turbulence promotes more efficient entrainment in stratocumulus than in smoke cloud. In a stratocumulus-capped boundary-layer, the generation of turbulent kinetic energy (TKE) by buoyancy fluxes is highly concentrated in the cloudy part of the layer, which is near the entrainment interface. This may focus the TKE near the entrainment interface and thereby promote efficient entrainment. Although the fourth explanation, like the second (mixing-induced evaporation), depends on the phase change of water, it is distinct. The fourth explanation suggests that entrainment into a boundary layer entirely filled with cloud would have a similar entrainment efficiency to a smoke cloud, while the second explanation predicts much higher entrainment efficiency for this case.

The plausibility of these explanations ranges from uncertain to improbable. Despite the aforementioned differences between the laboratory experiments and an atmospheric smoke-cloud, it seems unlikely that these could produce the tenfold difference in entrainment efficiency required by the first explanation. Shy and Breidenthal (1991) used nonlinearly mixing fluids as an analogue of evaporative cooling driven by cloud-top mixing. They stirred the lower layer in a density-stratified, nonlinearly mixing, two-layer system, and found little sensitivity of entrainment rate to the nonlinearity of the turbulent mixing ('evaporation') in a parameter range appropriate to stratocumulus layers, casting doubt on the second explanation. Many soundings through stratocumulus layers show a very sharp and strong inversion with an entrainment zone less than 50 m thick (Caughey *et al.* 1982). While the overlying air is often strongly stratified, the density change within the upper part of the entrainment zone above the inversion is usually substantially less than the density jump across the inversion. This makes it difficult to imagine a dynamical mechanism whereby the density structure of the inversion can affect the entrainment efficiency drastically as required by the third explanation. But one cannot rule this possibility out. In addition, the aircraft measurements of Nicholls and Leighton (1986), from which large A's were deduced, relied on high-resolution soundings in which an inversion jump was clearly identifiable and separable from the stratified layer above. Since there are no laboratory measurements of the turbulence structure in the smoke cloud, the most attractive test of the fourth explanation would be to compare the turbulence structure in numerical models of smoke and of stratocumulus clouds. This was not a part of the GCSS intercomparison, but is currently being examined by some of its participants.

The intercomparison described here focuses on the smoke cloud alone. Our main goal is to determine whether the different advection- and turbulence-schemes used in different models lead to substantial scatter in the predicted entrainment-rate and other turbulence statistics, for a numerical resolution typical of current LES studies of stratocumulus. The subsequent sections describe our intercomparison case and present a selection of results on the simulated boundary-layer structure. The entrainment scalings implied by the model results are then considered and compared with results from laboratory experiments, from the stratocumulus simulations described by Moeng *et al.* (1996) and from atmospheric observations.

2. Entrainment scaling

Inverse-Ri entrainment scalings of the form (1) have been proposed for a variety of related problems. In this section, we examine some heuristic arguments which lead to such scalings. LES simulations can also be used to test aspects of these arguments.

Consider the TKE budget in an entrainment zone near the top of an inversion-capped boundary-layer. In the entrainment zone, transport of TKE into the zone and possible shear-generation of TKE must balance entrainment, dissipation and storage. Dimensional arguments following Tennekes (1973) suggest that for a fully turbulent boundary-layer with velocity scale U and depth z_i, transport, dissipation and entrainment will all be of the order of (U^3/z_i). For a shear-driven boundary-layer, the shear production will also be of this order, while the storage term will be much smaller if the entrainment zone is strongly stratified. Hence, the entrainment buoyancy flux $\overline{w'b'}_e$ should scale as

$$-\overline{w'b'}_e = AU^3/z_i, \tag{3}$$

where A is an empirical constant. For a discontinuous inversion with a buoyancy jump Δb,

$$-\overline{w'b'}_e = w_e \Delta b. \tag{4}$$

By substituting (4) into (3) and expressing the result in terms of a bulk Richardson number $Ri = z_i \Delta b / U^2$, we obtain (1).

For buoyancy-driven boundary-layers, U can be taken as the convective velocity scale w_* (Deardorff 1980), defined from the vertically integrated generation of kinetic energy by buoyancy fluxes:

$$w_*^3 = 2.5 \int_0^{z_i} \overline{w'b'}\, \mathrm{d}z. \tag{5}$$

Observations of boundary layers driven by a surface flux penetrating into an overlying stable layer are generally consistent with the scaling (1). In this case, however, large undulations in the inversion hamper unambiguous sorting of the relatively small inversion jumps from the overlying stable stratification. Hence, values of A deduced from observations of cloud-free, convective boundary-layers show a fairly large degree of scatter; a typical value of about 0.2 is often quoted (Stull 1976). Interestingly, this value of A is similar to that found in the smoke-cloud laboratory-experiments.

Turner (1973) obtained a scaling of the same form as (1) but with w_* replaced by u_*, the friction velocity, for the case of a boundary layer driven by surface stress. Tank experiments by Kato and Phillips (1969) suggested that $A = 2.5$ for Richardson numbers $20 \leqslant Ri \leqslant 300$ but, again, values deduced from various other experiments exhibit a large scatter (Fernando 1991).

Other researchers have investigated the entrainment scaling when a turbulent layer below a stably stratified interface is internally stirred by an oscillating grid. The scaling appears to be Prandtl-number dependent. Turner (1968) found the scaling (1) also held for water stratified by heat. However, for water stratified by salt (which has a diffusivity 80 times smaller and would correspond to a Prandtl number of 600), he found that the entrainment efficiency was different. The laboratory experiments of E and Hopfinger (1986) verified this conclusion and found that w_e/U was actually proportional to $Ri^{-1.5}$ for the high Prandtl number case. Breidenthal (personal communication) suggested that even for high-Prandtl-number fluids, Turner's scaling should hold at the very high Reynolds numbers of the atmosphere, which are much larger than those attainable in the laboratory.

To date, there has been little effort to use large eddy or direct numerical simulations to test entrainment scaling relations, although the energetics of specific examples of the

above types of boundary layers have been examined in a variety of numerical studies. Current LES studies resolve the larger boundary-layer eddies well, but the entrainment interface is much less well resolved. This may impact estimates of entrainment rate by LES models and hence the physical relevance of LES-derived entrainment-scalings.

For boundary layers driven by surface heat flux, a comparison of four LES models (Nieuwstadt *et al.* 1992) showed quite good agreement of the buoyancy fluxes and the evolution of the inversion height, both between models and also with available observations. In such boundary layers, the entrainment interface is quite broad, filling 20–25% of the entire boundary-layer, and hence is easy to resolve. In the smoke-cloud case, the stability of the inversion is much stronger and the inversion is almost horizontal on the resolved scale of LES models. The smoke-cloud intercomparison aims to check how this affects the skill of LES models at predicting the overall entrainment rate, the turbulence structure within the layer and the structure of the entrainment interface itself. Another related study, based on a smoke-cloud idealization (Stevens and Bretherton 1999), examines how well an LES can reproduce the observed entrainment scaling as Ri is varied, and how this depends on the model resolution.

3. Description of the intercomparison case and participants' codes

The aim in developing the specification of the smoke-cloud simulations was to remain as close as possible to the basic configuration used for the first GCSS boundary-layer-cloud model intercomparison, while replacing the turbulence-generation mechanisms of the previous cloudy boundary-layer with a tightly-specified, idealized radiative forcing yielding cooling rates typical of stratocumulus.

The 'standard' model was prescribed as having a domain extent of 3.2 km in each horizontal direction and 1.25 km in the vertical. The domain was assumed to be horizontally periodic, with free-slip rigid surfaces at top and bottom, across which no scalar flux was allowed. The specified grid-spacing was 50 m in the horizontal and 25 m in the vertical. The whole domain was dry—that is, the total-water mixing-ratio was zero. The initial boundary-layer was assumed to be at constant potential temperature and uniformly filled with 'smoke' over its whole (700 m) depth. Above the inversion, the smoke concentration was set to zero, and a weak thermal stratification of 0.1 K km^{-1} was imposed in order to suppress subgrid-scale mixing. In order to allow for deviations from the basic grid-specification, the following continuous profiles of potential temperature (θ, K) and smoke concentration (S, nondimensional) were supplied.

For $0.0 \leqslant z \leqslant 687.5$

$$\theta = 288 \text{ K}$$
$$S = 1.$$

For $687.5 \leqslant z \leqslant 712.5$

$$\theta = 288 + 0.28(z - 687.5) \text{ K}$$

and

$$S = 1 - 0.04(z - 687.5).$$

For $712.5 \leqslant z \leqslant 1250.0$

$$\theta = 295 + 10^{-4}(z - 712.5)$$

and

$$S = 0.$$

Throughout the integration, S corresponds to the fraction of lower-layer fluid in any fluid parcel. The smoke is advected and mixed as a passive tracer and has no direct effect on the density. However, the vertical profile S determines the radiative cooling in a manner similar to the effect of liquid water on net long-wave radiation, as follows.

The radiative flux was calculated at levels midway between those on which S was held. Assuming the S-levels to be indexed by k, with $k + \frac{1}{2}$ being the fluid level halfway between S-levels k and $k + 1$, then for a specified radiative flux $F_0 (= F_{\text{ktop}+\frac{1}{2}})$ at the top of the domain,

$$F_{k+\frac{1}{2}} = F_0 \exp\left(- K_a \sum_{\ell=k+1}^{\ell=\text{ktop}} \rho_\ell S_\ell \Delta z \right). \tag{6}$$

If F_0 is specified in W m^{-2} then the associated rate of change of potential temperature is given by

$$\left(\frac{\partial \theta}{\partial t}\right)_k = -(F_{k+\frac{1}{2}} - F_{k-\frac{1}{2}})/(\rho_k C_p \Delta z).$$

In the above, ρ_k is the reference density at level k, Δz the vertical grid-spacing and C_p the specific heat of dry air at constant pressure. The smoke absorptivity K_a was chosen to be 0.02 m^2 kg^{-1}. Hence, a 44 m depth of undilute smoke (i.e. $S = 1$) would have unit optical depth. This absorptivity is comparable to that of a stratocumulus cloud with liquid-water content of 0.13 g kg^{-1} (Stephens 1978). While stratocumulus cloud tops usually have liquid-water contents higher than this, it was considered advantageous to distribute the radiative cooling over a thickness of cloud that could be resolved by our standard grid-spacing, so that poor resolution of the radiative-flux divergence would not be a major source of computational error. If F_0 is taken as 60 W m^{-2}, then the implied radiative-cooling rate at the top of the initial smoke-cloud is about 4 K h^{-1}.

For Boussinesq models, the reference density and potential temperature were assigned the constant values $\rho_0 = 1.1436$ kg m^{-3} and $\theta_0 = 291.5$ K respectively. In anelastic models, the reference density-profile was that corresponding to an isentropic atmosphere with $\theta = 291.5$ K. One Boussinesq-model code, that of the U.S. National Center for Atmospheric Research (NCAR), had a hard-wired reference density of 1 kg m^{-3}. In that case, to make the results as comparable as possible, the value of the reference density specified above was used in the radiative forcing and in the scaling of output fluxes where required, but its hard-wired value was retained elsewhere.

The reference surface-pressure was taken as 1000 hPa, the gas constant for dry air as 287 J kg^{-1} K^{-1} and C_p as 1004 J kg^{-1} K^{-1}. The Coriolis parameter was set to zero and there was no external forcing of momentum, no damping layer at the top of the domain, and no subsidence.

The resolved components of velocity were all zero at the initial time, when a spatially uncorrelated random perturbation, uniformly distributed between −0.1 K and 0.1 K was applied to the temperature field at all grid-points below 700 m. For those models which required it, the initial subgrid-scale TKE was specified as 1 m^2 s^{-2} everywhere below 700 m.

The standard requirement was that models should be run to simulate a period of 3 h, with production of specified time-series for the whole period, together with profiles of specified horizontal-mean quantities averaged over the third, final, hour. Participants were encouraged to extend their integrations beyond 3 h, if possible, to allow judgement of the representativeness of the standard results. From preliminary simulations carried out at the Meteorological Office (UKMO) and the University of Washington (UW), it appeared that the standard resolution might be too coarse to resolve the important scales of motion near

TABLE 1. PARTICIPATING SCIENTISTS

Scientists	Acronym	3-DS	3-DH	2-D	1-D
M. MacVean	UKMO	Y	Y	Y	
M. Wyant, H. Rand, C. Bretherton	UW	Y		Y	
D. Stevens, C. Bretherton	SB	Y			
C.-H. Moeng	NCAR	Y	Y		
B. Stevens	CSU	Y	Y	Y	
B. Kosovic, J. Curry	CU	Y			
J. Cuxart, J.-L. Redelsperger	MNH	Y			Y
A. Chlond	MPI	Y			
H. Cuijpers, P. Siebesma	IMAU	Y			
D. Lewellen	WVU	Y	Y		
I. Sykes	ARAP	Y	Y		
M. Khairoutdinov	UOK	Y			
P. Bechtold	AERO				Y

The acronyms are expanded in an appendix. They refer to the runs and code used by participating scientists, together with the type of runs they supplied. The latter are indicated by a Y in columns 3 to 6. 3-DS and 3-DH denote three-dimensional runs at standard and high vertical resolution respectively.

the top of the boundary layer adequately. Higher-resolution simulations were solicited from those groups which had the available computer resources.

It was felt important to include one- and two-, as well as three-dimensional simulations of the same basic case. Because of the vast computer resources required for high-resolution 3-D simulations, many studies are carried out with 2-D models and it is essential to determine in what respects predictions from such studies can be regarded as realistic. The ultimate aim of intercomparison studies such as this is to provide better parametrizations of the boundary layer for use in larger-scale models. For our purposes, a large-scale model can be regarded as a horizontal array of 1-D models and so it is important to understand the current strengths and weaknesses of 1-D models when applied to the intercomparison cases.

Thirteen groups submitted model results, and some of them submitted more than one set (see Table 1). The abbreviations used in Table 1 are expanded in an appendix. All but one of the groups provided results from 3-D models at the standard resolution, while five of them also provided corresponding results obtained using a vertical resolution around the inversion that was at least twice as good as in the standard case, while retaining the standard horizontal resolution of 50 m. Two of these groups (CSU and NCAR) used a uniform vertical grid-spacing of 12.5 m; the other three groups employed stretched grids that had a minimum grid-spacing of 5 m at a height of 700–725 m and slowly increased to a maximum of 25 m far from this height. Three groups submitted data from 2-D models and two groups provided results from 1-D simulations. In their 1-D model, MNH used the same differencing algorithms and subgrid-scale-turbulence scheme as in their 3-D model.

Most of the model codes were developed independently. Even those with common roots (WVU and ARAP; NCAR and CU) have since diverged to the point where they can no longer be regarded as the same. All the 3-D and 2-D codes solved the non-hydrostatic incompressible equations with either the Boussinesq or the anelastic approximation. Test simulations of the smoke-cloud case using these alternative approximations in otherwise identical models have shown no significant sensitivity to the choice made. The AERO 1-D code was alone in integrating a hydrostatic, compressible equation set.

Finite differences were used by the majority of the groups to solve the equations, the exceptions being NCAR and CU, who used pseudo-spectral methods in the horizontal

TABLE 2. SOME KEY CHARACTERISTICS OF THE MODEL CODES

Code (1)	Type (2)	Approximation (3)	SGS closure (4)	MSA (5)	MMA (6)	Time-step (sec) (7)
UKMO-N	FD	Boussinesq	Smagorinsky–Lilly			0.6*
UKMO-M	FD	Boussinesq	Smagorinsky–Lilly	Y		0.8*
UW	FD	Anelastic	Smagorinsky–Lilly	Y		5
SB	FD	Anelastic	None	Y	Y	5
NCAR	SP-FD	Boussinesq	TKE–Deardorff			0.5
CSU	FD	Anelastic	Smagorinsky–Lilly	Y		2
CU	SP-FD	Boussinesq	TKE–Deardorff			2
CU-NL	SP-FD	Boussinesq	TKE–nonlinear			2
MNH	FD	Anelastic	TKE			5
MPI	FD	Boussinesq	TKE–Deardorff	Y		3
IMAU	FD	Boussinesq	TKE–Deardorff	Y		1
WVU	FD	Boussinesq	TKE–ARAP	Y		3*
ARAP	FD	Boussinesq	TKE–ARAP	Y		4
UOK	FD	Boussinesq	TKE–Deardorff	Y		2
AERO	FD	—	TKE	—	—	40

In column 2, FD stands for finite difference and SP-FD for mixed finite-difference/spectral. A Y-entry in columns 5 or 6 indicates that the code has monotone scalar-advection (MSA) or monotone momentum-advection (MMA) respectively. Column 7 gives the time-step in seconds for 3-D runs at the standard resolution; an asterisk indicates a typical value in a code that uses a variable timestep.

and finite differences in the vertical. A wide variety of numerical advection techniques was used, ranging from straightforward space- and time-centred schemes to sophisticated, higher-order, upwind-biased ones. It is not possible to document all the features of these schemes here; Table 2 lists certain key characteristics but for fuller details, the reader is referred to the references given in the appendix. For our purposes, it is sufficient to categorize multidimensional codes according to whether or not advection is monotone (i.e. whether or not the advection update preserves the range of the variable being updated). This property is listed separately for scalars and momentum in Table 2. Most of the advantages of monotone advection-schemes are obtained when they are applied to scalars. Only one group (SB) also enforced monotonicity in the advection scheme for momentum. In view of this, we will describe a code as monotone (M) or non-monotone (N) on the basis of the scalar-advection properties alone.

Four of the groups used subgrid-scale-turbulence schemes based on the first-order closure originally proposed by Smagorinsky (1963) and later extended by Lilly (1967). All but one of the others used higher-order closures, incorporating an equation for the subgrid-scale TKE. The majority of these followed the approach of Deardorff (1980), the exceptions being ARAP and WVU (who both used the ARAP closure of Sykes and Henn (1989)), MNH and AERO. The MNH model was unique in computing a turbulent subgrid-scale Prandtl number dynamically instead of specifying a constant turbulent Prandtl-number. For a discussion of the basic properties of the above schemes, the reader is referred to Moeng *et al.* (1996) and Cuxart (1997). SB took the radical step of dispensing with a subgrid model altogether, relying instead on the advection scheme to provide the necessary dissipation implicitly.

Finally, the wide range of time-steps used in the different codes should be noted. This wide range arises out of the different stability constraints of the numerical methods used. The factor of ten between the smallest and the largest time-step raises the possibility of significantly different temporal truncation-errors in the different simulations, but this has not been investigated.

4. Intercomparison results—time-series, fields and profiles

In this section, only a small part of the data collected in the intercomparison can be discussed. A comprehensive collection of the results is available on the World Wide Web at http://www.amath.washington.edu/~breth/GCSS/GCSS.html).

In the simulations, the boundary-layer depth z_i is defined as the height of the $S = 0.5$ surface, horizontally averaged over all columns. In each column, this height is found by linear interpolation between the highest level at which S exceeds 0.5 and the next-higher level. The attractions of this choice are threefold. Firstly, this surface remains in the centre of the entrainment zone, which is characterized by mixtures of lower and upper fluid. Secondly, uniform diffusion of a sharp interface between undilute upper and lower fluids would not affect the height of this surface (in the absence of top and bottom boundary effects). Thirdly, the value chosen in this way changes more linearly with time than any other measure we have experimented with, allowing the entrainment rate to be estimated with more confidence. Entrainment rate is calculated as the time derivative of z_i.

(*a*) *Evolution*

(i) *Entrainment.* Firstly, we investigate how long it takes for a regime of nearly steady-state convection and entrainment to develop in response to the radiative forcing, starting from quiescent initial conditions. Time series of values of z_i are shown in Fig. 1, with separate panels for the following groups of integrations: three-dimensional, high resolution (3-DH); three-dimensional, standard resolution with non-monotone advection (3-DN) or monotone advection (3-DM); two-dimensional (2-D) and one-dimensional (1-D). For many of the models, z_i rises fairly linearly with time (steady entrainment) after approximately one hour. However, all members of 3-DN, except one, continue to show a tendency for the entrainment rate to increase with time. Some of the 1-D and 2-D models also have significant oscillations in the entrainment rate, making determination of a time-average entrainment rate more uncertain.

We estimate a 'steady-state' w_e by the average rate of rise of z_i over the third hour of each model run. Since entrainment is a central focus of this paper, we try to quantify how representative this estimate is. For the standard- and high-resolution UKMO-M model, the simulation was extended to 4 h. In the high-resolution simulation, the hourly average w_e differs by only about 1% between the third and fourth hours of the simulation. At standard resolution (25 m grid spacing), w_e varies by about 10% between the third and fourth hours. Two other groups have also supplied entrainment rates for the fourth hour, both from standard-resolution runs. In one case the differences between average rates for the third and fourth hours are about 19%, and in the other case about 37%.

As we shall illustrate below, the horizontal variation of inversion height in the standard run is substantially less than one grid-spacing. Hence, one might expect the entrainment rate to be affected as the inversion moves across a particular grid-level on many grid-columns at the same time. This behaviour produces oscillations in the rise rate of z_i evident in the 1-D models. Similar, but less prominent, oscillations are also noticeable in the two 3-DH models with the coarsest vertical grid-spacing of 12.5 m (CSU and NCAR). In the standard-resolution models, it takes 2–3 h (the full length of a model run) to raise the inversion one 25 m grid spacing, so it is harder to identify such oscillations. However, they may produce some of the hour-to-hour variation in w_e, suggesting that an averaging period of as much as 3 h would be useful in order to produce a more stable estimate of w_e. In 3-DH runs with 5 m vertical grid-spacing, the inversion passes through almost two grid-levels per hour, so there is no advantage in averaging w_e for more than an hour.

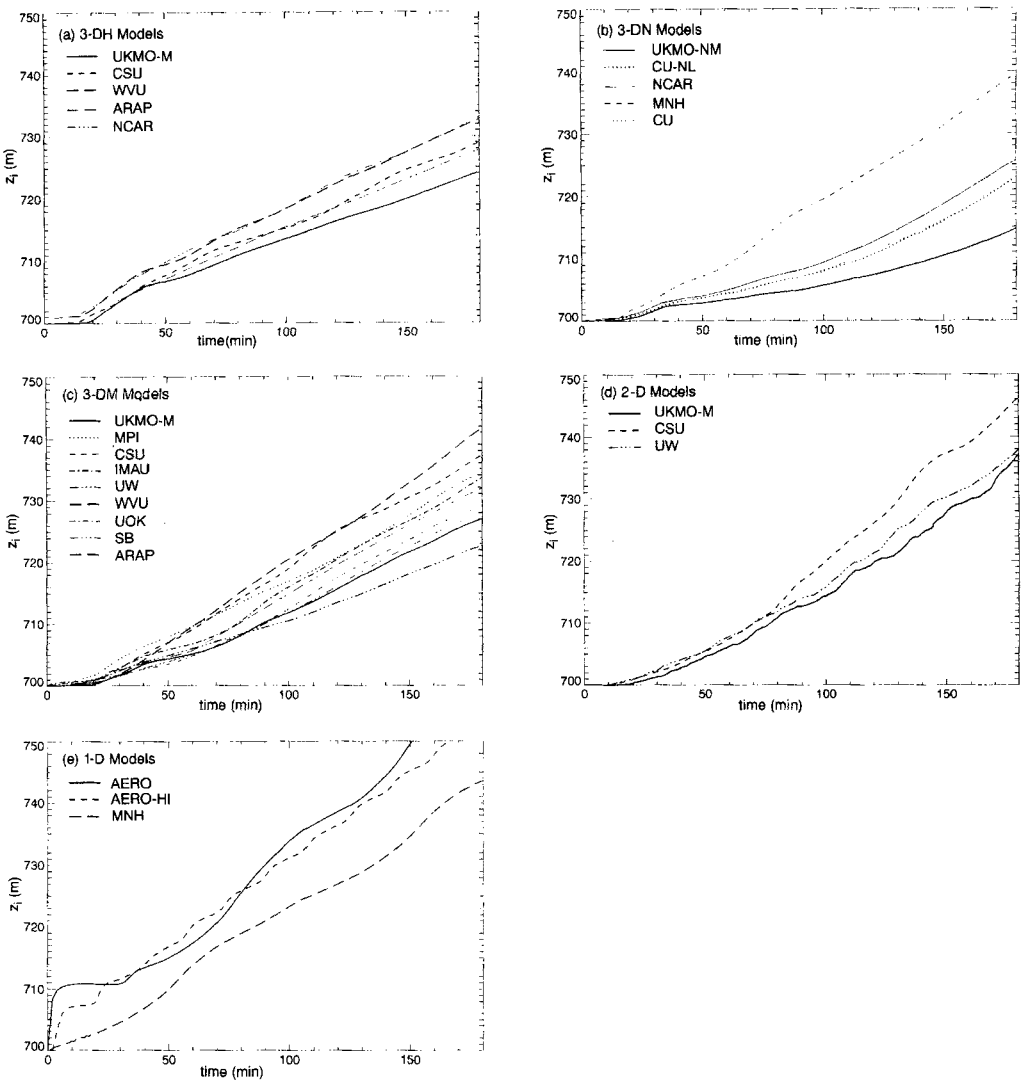

Figure 1. Time series of values of z_i for 0–3 h for all models, displayed by group: (a) 3-DH; (b) 3-DN; (c) 3-DM; (d) 2-D; (e) 1-D.

On the basis of the discussion above, one should assume that the uncertainty in the representativeness of an hourly average entrainment-velocity is at least 10% and possibly significantly more for some of the standard-resolution runs.

(ii) *TKE and buoyancy fluxes.* Figure 2 shows the corresponding time-series of TKE (resolved plus subgrid) averaged over the depth of the boundary layer (TKE_{blav}). The behaviour of TKE_{blav} near the start of the integration was dependent on the model subgrid-scale turbulence-scheme. For those models with a first-order turbulence-closure, TKE_{blav} is small near the beginning of the run, reflecting the small velocities resulting from the small initial temperature-perturbation. Models with a TKE closure have a considerable imposed initial subgrid TKE of 1 m^2 s^{-2}, but TKE_{blav} falls rapidly over the first 15 minutes, to values comparable with those in the other models. The most prominent characteristic of the subsequent development of TKE_{blav} in the 3-D runs is a damped oscillation with a

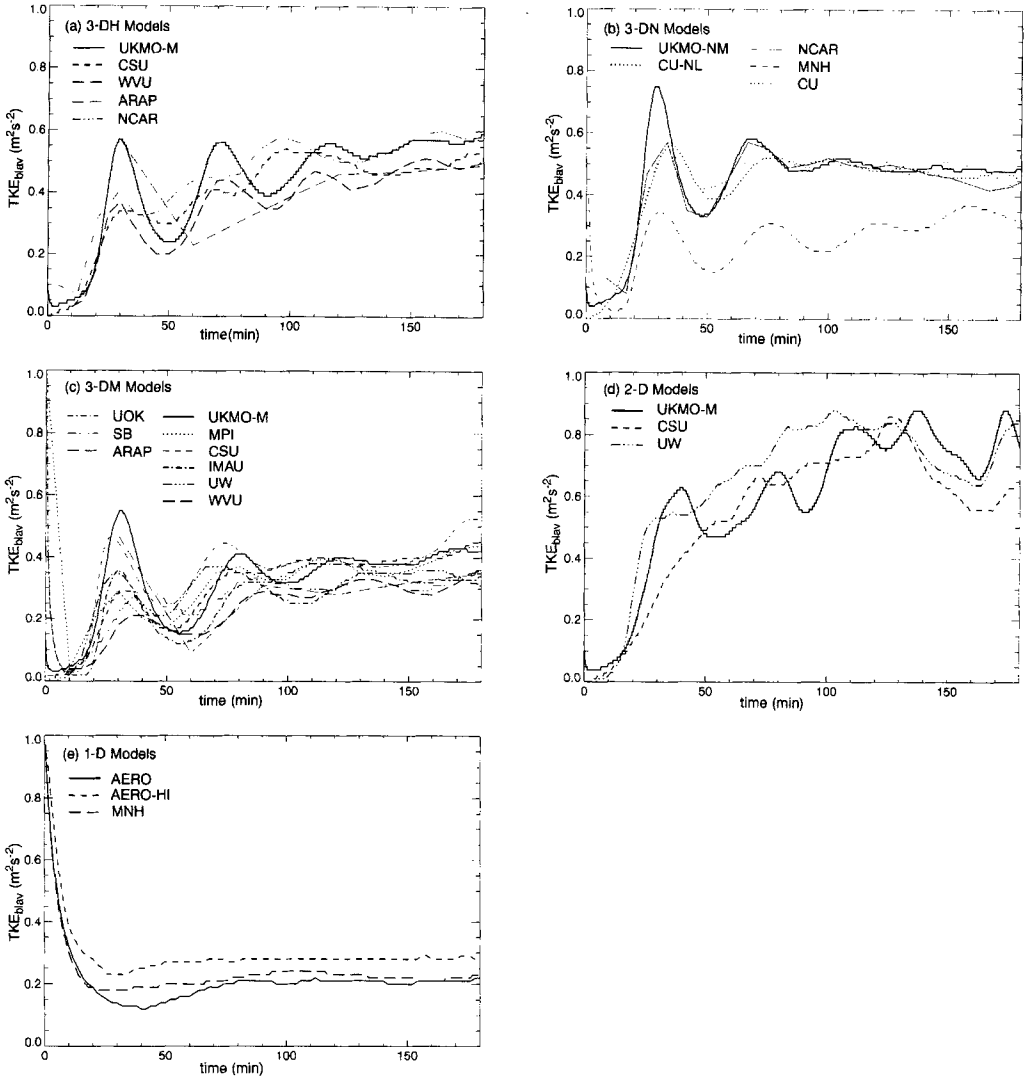

Figure 2. Time series of TKE_{blav} for 0–3 h for all models, displayed by group: (a) 3-DH; (b) 3-DN; (c) 3-DM; (d) 2-D; (e) 1-D. ARAP 3-DM TKE_{blav} was provided only every 30 minutes.

period of about 40 min. The amplitude of this oscillation is, however, generally small over the period 120–180 min, which was used for collecting statistics. The time-series provide evidence that this is a period of approximate statistical equilibrium for most 3-D models, though there is still a slight upward trend in TKE_{blav} in the 3-DH and 3-DM models. The 2-D models all have a somewhat less regular, less damped TKE_{blav} oscillation, with values of TKE_{blav} between two and three hours that are 50% larger than in the 3-D runs. The 1-D models settle to nearly steady TKE_{blav} within the first hour but at rather lower levels than in the 3-D runs.

The primary source of TKE is the boundary-layer averaged heat-flux (not shown). In the 3-D models, this heat flux also has 40-minute oscillations which are more weakly damped than in TKE_{blav}, and the heat flux varies by $\pm 20\%$ in the 2–3 h interval. These oscillations add variability of $\pm 10\%$ or more to the hourly averages of statistics related to

TABLE 3. 2–3 HOUR AVERAGES OF SELECTED MODEL PARAMETERS (MKS UNITS) DESCRIBED IN TEXT

CODE	$w_e * 10^3$ (mm s^{-1})	$\sqrt{TKE_{blav}}$ (m s^{-1})	w_* (m s^{-1})	A	F_{above} (W m^{-2})
UKMO-M	2.20	0.743	0.948	0.47	0
CSU	2.90	0.698	0.908	0.70	0
WVU	2.89	0.686	0.890	0.74	0
ARAP	2.58	0.687	0.917	0.60	0
NCAR	2.85	0.744	0.885	0.76	6
UKMO-M	3.16	0.632	0.825	1.01	0
MPI	3.80	0.618	0.801	1.33	0
CSU	3.39	0.633	0.772	1.32	0
UOK	3.19	0.647	0.797	1.12	0
IMAU	3.66	0.577	0.749	1.55	0
UW	2.57	0.594	0.889	0.64	12
SB	3.11	0.561	0.864	0.86	0
WVU	4.64	0.560	0.714	2.27	0
ARAP	3.42	0.563	0.771	1.32	0
UKMO-N	2.05	0.697	0.956	0.43	3
NCAR	3.62	0.679	0.839	1.13	4
MNH	4.25	0.572	0.789	1.58	1
CU	3.25	0.696	0.838	1.01	6
CU-NL	3.45	0.688	0.852	1.02	6
UKMO-M	4.81	0.884	0.639	3.29	0
CSU	5.58	0.821	0.529	6.75	0
UW	4.65	0.863	0.764	1.82	8
AERO	6.07	0.457	0.557	6.31	0
AERO-HI	4.81	0.531	0.700	2.54	0
MNH	4.59	0.470	0.722	2.22	0

Blank lines separate groups of runs, in the order 3-DH, 3-DM, 3-DN, 2-D and 1-D.

heat flux, such as the convective velocity scale w_*, even after 2–3 h of simulation. The 2-D models tend to have shorter but larger and more irregular heat-flux oscillations of ±100%, while the 1-D models settle to a stable heat-flux within an hour.

(b) *Comparison of 2–3 hour average entrainment rate and* TKE_{blav}

Table 3 lists the 2–3 h averages of a few important parameters for all models. These include w_e and TKE_{blav} (discussed in this subsection), a radiative cooling parameter F_{above} (to be discussed in subsection 4(d)), w_* (discussed in subsection 4(e)), and derived entrainment efficiency A (discussed in subsection 4(f)).

Figure 3 shows the 2–3 h average entrainment rate and TKE_{blav} for the models, partitioned by group. The hatched zone in Fig. 3(a) is the range of entrainment rates

$$w_e = \frac{1.25A}{1 + 1.25A} \frac{gF_0[1 - \{2/(K_a\rho_0 z_i)\}]}{\rho_0 C_p \theta_0 \Delta b}, \tag{7}$$

that one would obtain from using a mixed-layer model using entrainment closure (1) with A in the range 0.2–0.4 suggested by the laboratory experiments. Here, the values

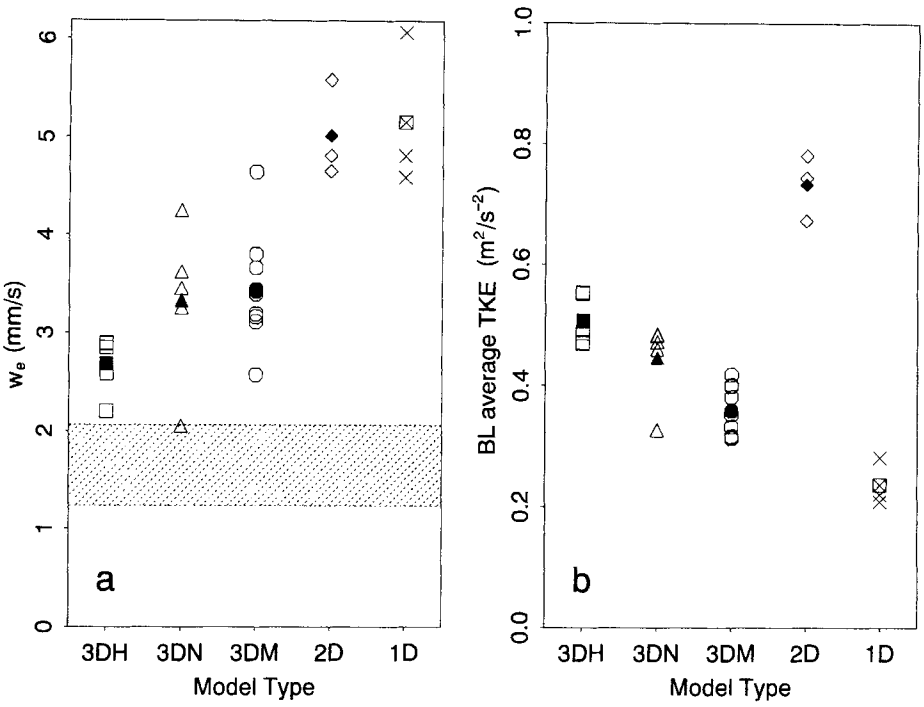

Figure 3. 2–3 h averages, partitioned by group: (a) w_e; (b) TKE_{blav}. Filled symbols (crossed square for 1-D) indicate means for each group. Hatched zone in (a) indicates prediction based on laboratory analogue.

$z_i = 725$ m and $\Delta b = 0.25$ m s^{-2} are representative of the inversion height and the horizontally averaged buoyancy-jump across the inversion during the 2–3 h interval. To obtain (7), we make the approximation that $S = 1$ below the inversion and $S = 0$ above the inversion, use the specified profile of radiative flux (6), and use this to determine the dependence of the buoyancy flux profile and hence w_* on w_e (see (11)). We then set $U = w_*$ in (1) and solve for the entrainment rate.

In general, models within each group approach comparable steady-state entrainment-rate and TKE_{blav}, regardless of the details of their advection and subgrid-scale-turbulence schemes. One exception is the MNH model, which was an outlier among the 3-DN models in both w_e and TKE_{blav}. The results from MNH are, in many respects, more comparable with those in 3-DM; the reason for this is not clear. The MNH model has since been found to give similar results with a monotone advection-scheme. The dynamically varying turbulent Prandtl number used by MNH may contribute to these results, but this has not been fully investigated.

Of the 3-D models, the high-vertical-resolution models have the highest TKE_{blav} (0.5–0.6), followed by the 3-DN models (0.4–0.5), then the 3-DM models (0.3–0.5). The 3-DH models have 10–50% higher entrainment rates than the upper bound of the laboratory-predicted range. On average, the 3-DM and 3-DN standard-resolution models have 25% higher 2–3 h entrainment rates than the 3-DH models. It should be remembered that, in all but one of the 3-DN models, the entrainment rate increases with time (Fig. 1), with considerably lower values in the first two hours than in the third.

We did not see obvious systematic differences in entrainment rate or TKE_{blav} between the three high-vertical-resolution models that used a stretched grid with high resolution only near the inversion and the two high-resolution models (NCAR and CSU) that used

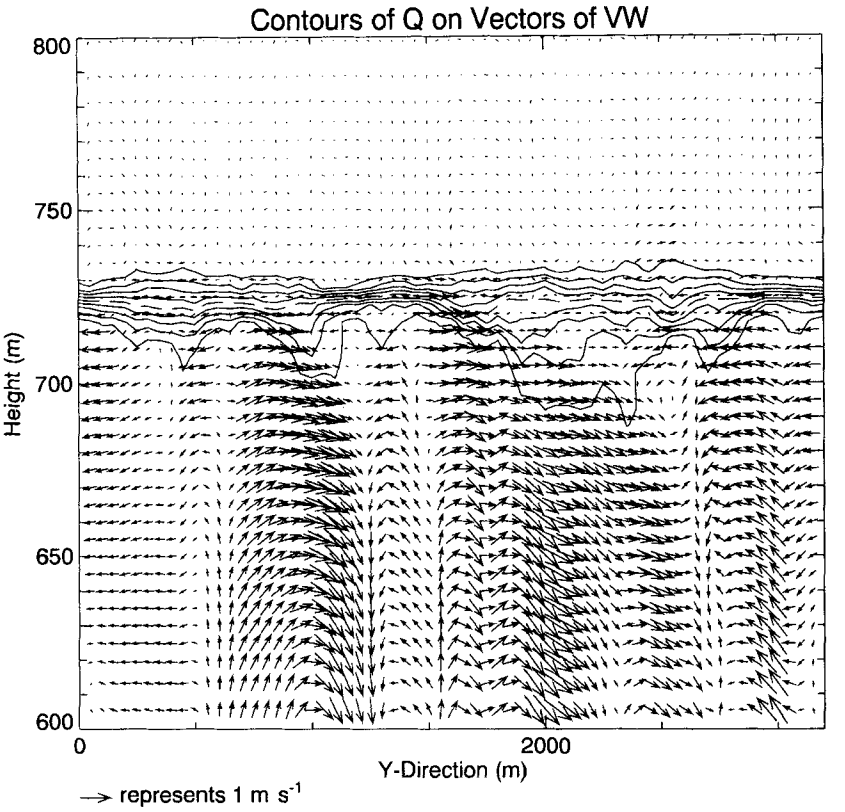

Figure 4. Velocity vectors in the vertical plane at $x = 0$, and smoke concentration (contours from 0.1 to 0.9 with interval 0.1) for UKMO-M model using high (5 m) vertical resolution.

uniformly high vertical resolution. This suggests that to obtain more accurate entrainment rates, it suffices to use high vertical resolution only in and near (i.e. within 50–100 m of) the inversion.

The 2-D models maintain much higher TKE_{blav} (≈ 0.8) and larger entrainment rates, while the participating 1-D models have much lower TKE_{blav} but even higher entrainment rates.

(*c*) *Inversion structure and vertical resolution*

In Figs. 4 and 5 we present typical vertical cross-sections of the structure of the inversion after three hours from UKMO-M runs at high and standard vertical resolution respectively. Velocity vectors are superimposed on contours of S. In the region shown, the high resolution run has a vertical grid-spacing of 5 m. The most obvious difference between the runs is in the inversion thickness, which we define as the height between the $S = 0.9$ and 0.1 contours (the lowest and highest contours on the cross-sections). In both runs, there are locations where the inversion thickness is less than $2\Delta z$. However, this is true for a much larger fraction of the columns in the standard-resolution run than in the high-resolution run. The mean inversion thickness in the standard resolution run (50 m) is three times as large as in the high-resolution run. In the high-resolution run there is also much more pronounced horizontal variability in the sharpness of the inversion associated with updraughts and downdraughts. The horizontal variability of boundary-layer depth σ_S (defined as the standard deviation of the height of the $S = 0.5$ contour from its horizontal

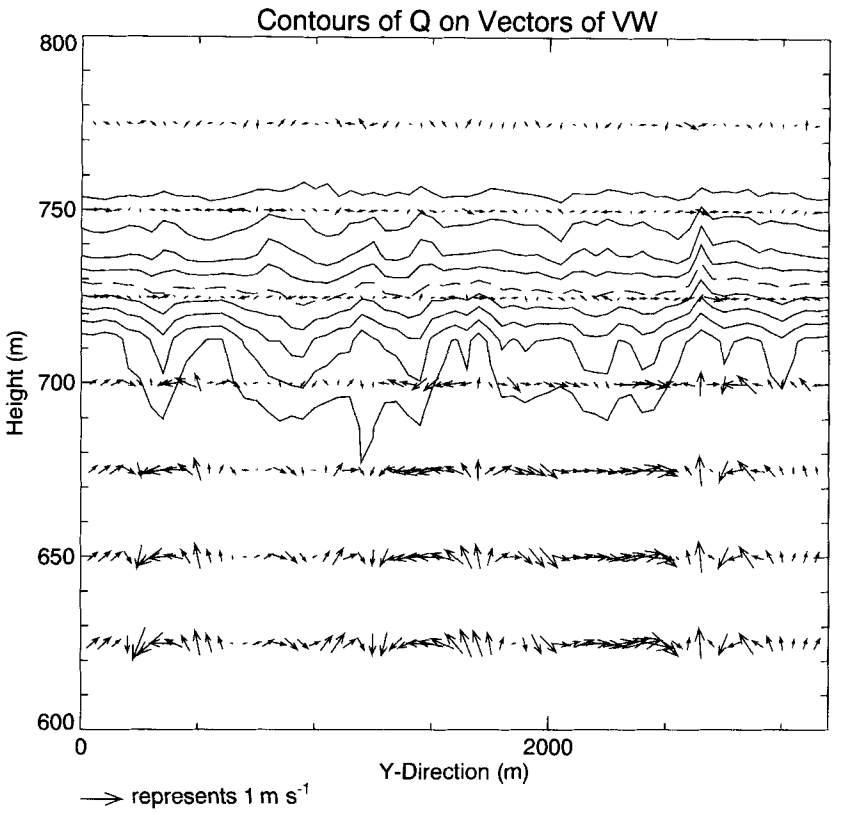

Figure 5. As Fig. 4, but using standard (25 m) vertical resolution.

average) is also poorly resolved with standard resolution. It is about 11 m, which is less than half the grid spacing. At high vertical resolution, σ_S is 6 m, only half as large as at low resolution and slightly larger than the grid length. From this comparison, we conclude that the standard 25 m vertical grid-spacing seriously underresolves the inversion and misrepresents both its mean structure and its variability. With 5 m vertical grid-spacing, these aspects of inversion structure are better resolved. We do not know if further improvements in vertical resolution would significantly change the predicted horizontal variability in inversion structure.

Good resolution of the inversion mixing-zone promotes a more accurate prediction of bulk entrainment rate, firstly by improving the representation of entrainment dynamics (and decreasing spurious numerical diffusion) and, secondly, by better representation of the distribution of radiative cooling within and below the mixing zone. The intercomparison study did not attempt to untangle these two effects, though studies in progress by participants will do so.

A scaling argument suggests the vertical grid-spacing required to resolve the inversion-height variability. If a convective updraught with a velocity scale w_* impacts on an inversion with a buoyancy jump Δb across it, then because of the inertia and negative buoyancy of the parcel, a characteristic height scale for inversion deformation or undulation is

$$\delta z_u = w_*^2/\Delta b. \tag{8}$$

A similar argument suggests that, in the absence of mean vertical shear of the horizontal

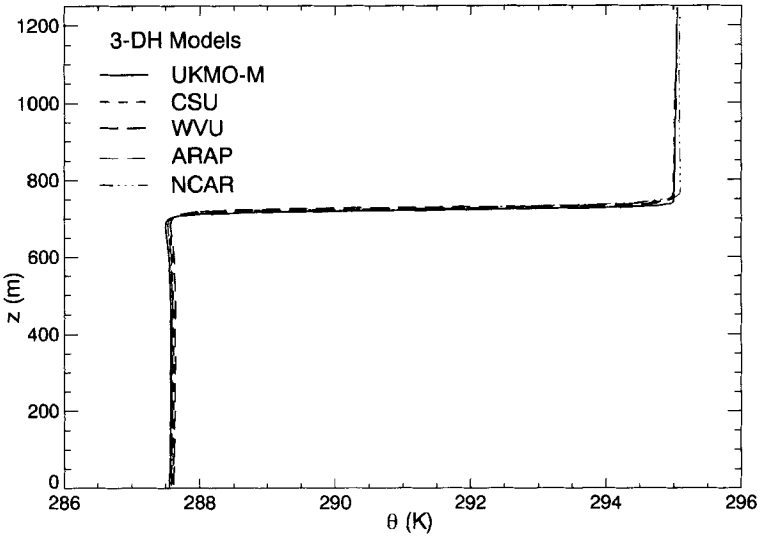

Figure 6. Vertical profile of θ, averaged over 2–3 h for 3-DH models.

wind, the typical inversion thickness δz_i may also scale with δz_u. Across the inversion zone, the buoyancy jump is Δb, and there will typically be a velocity jump of the order of w_* as a result of eddy motions below the inversion. Kelvin–Helmholtz instability would lead to thickening of the inversion if the shear Richardson number in the inversion, which scales with $\delta z_i \Delta b / w_*^2 = \delta z_i / \delta z_u$, is less than 1/4. This keeps values of δz_i of the same order as values of δz_u, or larger, in most vertical columns.

For the GCSS case, $w_* \approx 0.9$ m s^{-1} and $\Delta b = 0.25$ m s^{-2}, so $\delta z_u \approx 3$ m. This is a conservative estimate; δz_u is only half the value of σ_S found in the high resolution UKMO model. We hypothesize that a vertical grid-spacing comparable to or smaller than δz_u is necessary to resolve the horizontal variability in inversion height and entrainment-zone thickness, and produce a correct entrainment-rate. While it is not clear that any of the 3-DH models meet this requirement, those with 5 m vertical grid-spacing are close. This argument does not predict the required horizontal grid-spacing near the inversion.

These scaling arguments also apply to cloud-capped boundary-layers. The GCSS case has a w_* and inversion strength that are similar to those associated with subtropical marine stratocumulus-capped boundary-layers. Hence, we believe that the 25–50 m vertical grid-spacing that has been used in most recent studies of such boundary-layers is likely to lead either to model-dependent overestimates of entrainment or underestimates of $\mathrm{TKE}_{\mathrm{blav}}$ of up to 50%. For boundary layers with a weaker inversion, with stronger convection, or with wind shear at the inversion to induce large-amplitude Kelvin–Helmholtz instability, the requirements on vertical resolution may become considerably less stringent.

(*d*) *Profiles of θ, S, and their fluxes*

Figures 6 and 7 show the horizontal-mean profiles of θ and S, averaged over the period 2–3 h for 3-DH. All models maintain nearly well-mixed profiles of θ and S, and the differences between the individual models are small. The slight curvature in the θ-profile below the inversion reflects the radiative forcing. The 3-DM and 3-DN profiles (not shown) are similar, except that the thickness of the inversion layer is larger. In the 2-D and 1-D runs, the S-profiles (not shown) are slightly less well mixed than in 3-DH.

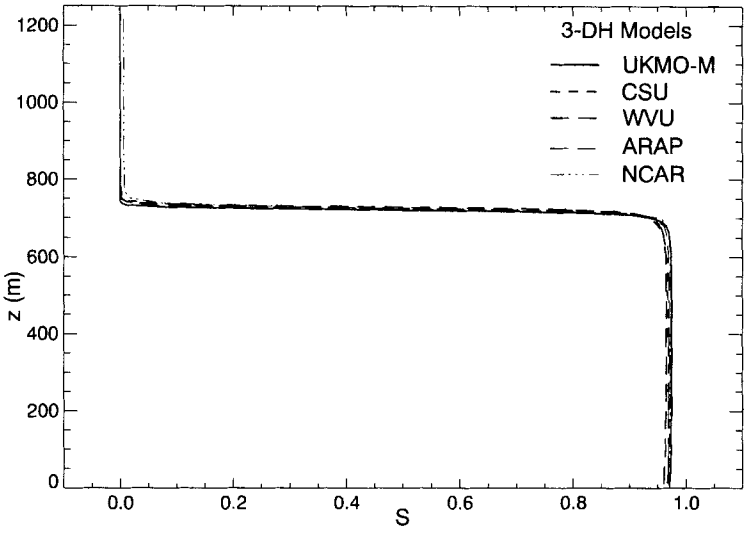

Figure 7. Vertical profile of S, averaged over 2–3 h for 3-DH models.

The mean boundary-layer temperature in 2-D and 1-D is typically a few tenths of a Kelvin warmer and S a few per cent lower than in 3-DH, reflecting the greater entrainment of warm, clear air from above.

The inter-run variation in the smoke profiles for 3-DN was about twice that in any of the other 3-D groups. This behaviour is related to undershoots and overshoots generated by the advection schemes and to the different patches applied to the smoke field in the various models to minimize their effect. These created spurious changes in the fields above the inversion that are especially evident in the NCAR model.

Although the intention was that all integrations should be driven by a radiative flux of 60 W m^{-2} at the top of the *boundary layer*, this radiative forcing was specified at the top of the *domain*. In some of the runs, the smoke mixing-ratio above the inversion was significantly different from zero. As shown in Table 3, these models had significant flux-divergence F_{above} above the inversion. Such behaviour might be expected for models using a non-monotone advection-scheme. However, the largest above-inversion flux-divergence, of 12 W m^{-2} (20% of the overall radiative cooling, and twice as much as in any other model), was seen in the UW model, which uses a monotone advection-scheme. This model used a Smolarkiewicz–Clark (1986) nonlinear advection-scheme for scalars. By making the scheme more diffusive when there is a sharp gradient in scalar concentrations with near-zero concentrations on one side, this advection scheme guarantees that scalar values do not become negative. The implementation of this scheme in the UW model (where it is used in addition to flux correction) seems much more diffusive for smoke concentration at the inversion than flux correction applied to the high-order advection-schemes used in other monotone models.

In Fig. 8 we show the convective heat-flux (resolved plus subgrid) for all the runs in the various groups. There is good qualitative agreement between the individual runs in 3-DH, with the exception of the spurious positive flux above the inversion in NCAR. This positive flux results from overshoots of θ just above the inversion due to the non-monotone advection-scheme. This creates an unstable stratification just above the inversion. Since the above-inversion layer is almost unstratified, the resulting convection extends through the entire above-inversion layer.

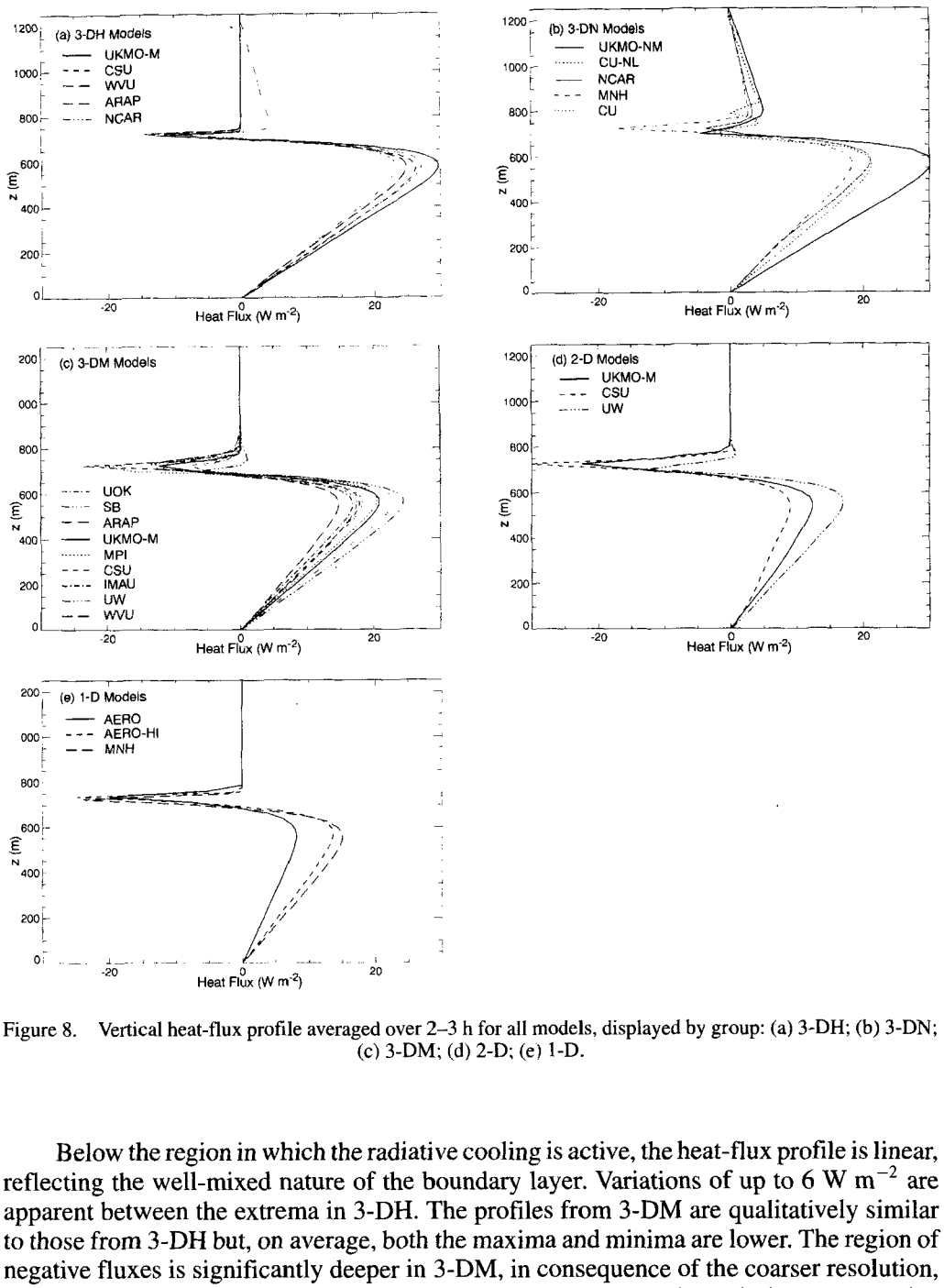

Figure 8. Vertical heat-flux profile averaged over 2–3 h for all models, displayed by group: (a) 3-DH; (b) 3-DN; (c) 3-DM; (d) 2-D; (e) 1-D.

Below the region in which the radiative cooling is active, the heat-flux profile is linear, reflecting the well-mixed nature of the boundary layer. Variations of up to 6 W m^{-2} are apparent between the extrema in 3-DH. The profiles from 3-DM are qualitatively similar to those from 3-DH but, on average, both the maxima and minima are lower. The region of negative fluxes is significantly deeper in 3-DM, in consequence of the coarser resolution, while the scatter in the minima is very large. This scatter may not be entirely representative of a longer-term average, as it may also reflect the different 2–3 hr mean height of the inversion in different models with respect to grid levels, as well as temporal variability in the buoyancy fluxes. Comparing 3-DM and 3-DN, we find that the significant differences are largely confined to the uppermost part of the boundary layer and above. Spurious positive fluxes are seen above the inversion in 3-DN, while the magnitude of the flux minimum is generally much reduced. The values of the fluxes at the inversion in MNH are

nearer to those in 3-DM than to those in the other 3-DN models, in spite of the evidence of non-monotone advection in its flux profile higher up. The profiles from 2-D and 1-D runs compared well, although both the maxima and minima were, on average, lower than those in the 3-D simulations. Comparing 1-D or 2-D with 3-DH, we see that the magnitude of the minimum in the former is about twice that in 3-DH, while the magnitude of the maximum has approximately halved. This constitutes a very significant difference in the distribution of the heat flux over the boundary layer.

The shape of the heat-flux profile can be understood by idealizing the smoke layer to be a mixed layer. In this case, the sum of the convective heat flux and the net radiative flux must vary linearly up to the inversion to keep the tendency of θ the same at all heights in the mixed layer. The convective heat flux at $z = 0$ is zero as a result of the surface boundary-condition. Furthermore, the optical depth of the smoke over the entire domain depth in all model runs is approximately 16, so the net radiative flux at $z = 0$ is negligibly small. At the smoke-layer top, the convective heat flux is $-\rho C_p w_e \Delta\theta$, as a consequence of entrainment, while the radiative flux is F_0 (assuming no smoke has been spuriously created above the inversion by the model). Thus, at any height in the smoke layer, the convective heat flux $H(z)$ is

$$H(z) = \rho C_p \overline{w'\theta'}(z) = -F(z) + \left(\frac{z}{z_i}\right)(-\rho C_p w_e \Delta\theta + F_0). \tag{9}$$

The radiative flux as a function of height can be calculated using (6). The calculation can be carried out in closed form by assuming that the boundary layer is well mixed with a constant density ρ_0 and a smoke mixing-ratio close to 1, in which case

$$F(z) = F_0 \exp\{-\rho_0 K_a (z_i - z)\}. \tag{10}$$

Even for models using the anelastic equations, these assumptions produce negligible errors in the radiative-flux profile. Substituting (10) into (9) we see that the heat-flux profile for the mixed-layer model depends primarily on the entrainment rate. In Fig. 9 we show the 2–3 h average convective heat flux, the radiative flux, and their sum from the high-resolution UKMO-M run. We also show the mixed-layer prediction of the heat-flux profile from (9), using the model-deduced $w_e = 2.20$ mm s^{-1} and $z_i = 720$ m. This prediction agrees closely with the LES-calculated heat-flux profile at all heights, confirming that the mixed-layer approximation is quite good for inferring some of the energetics of the smoke layer. The linearity of the sum of the convective heat flux and the radiative flux in the smoke cloud is also consistent with the smoke cloud acting as a mixed layer.

Figure 9 also shows the subgrid contribution to the convective heat flux. It is largest a short distance below the inversion, but, even there, it is still small compared with the maximum resolved heat-flux just below the inversion. One might be tempted to conclude that the turbulent circulations are well resolved (and therefore trustworthy), even at the entrainment interface. However, as we have seen in Fig. 4, the inversion in this model is rather flat, even with 5 m vertical grid-spacing. Hence, 'entrainment' through the inversion must rely heavily on numerical and subgrid-scale diffusion, rather than the advection of discrete tongues of clear air into the smoke layer, and we should not be overconfident that the entrainment process is correctly represented. The same would be even more true for cloud-topped boundary-layers, where evaporation, microphysics and radiation are tightly coupled to the entrainment dynamics.

Figure 10 shows the total smoke-flux for 3-DH only. In a mixed layer, the smoke flux would increase linearly from zero at the base to $-w_e \Delta S$ at the top, capped by a sharp decrease to zero at the inversion. All the 3-DH models are qualitatively consistent with

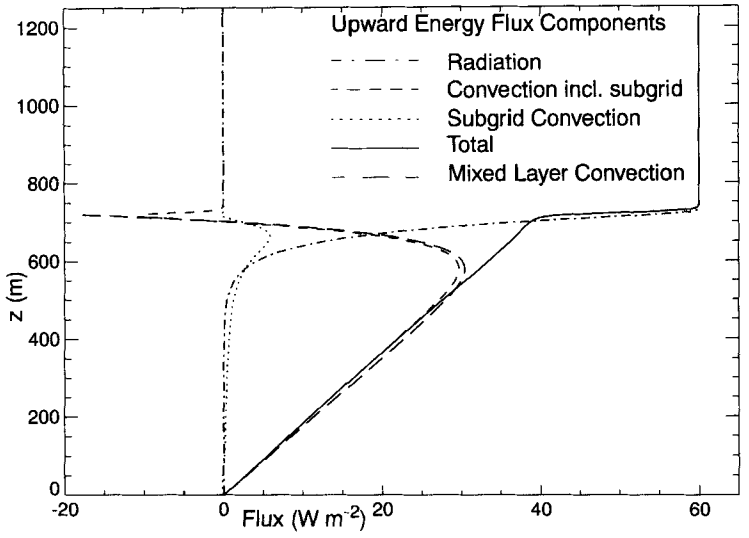

Figure 9. Profiles of radiative flux, convective heat flux, subgrid component of the convective heat flux, sum of the radiative and convective heat fluxes from the UKMO 3-DH model, together with mixed-layer prediction of the convective heat flux.

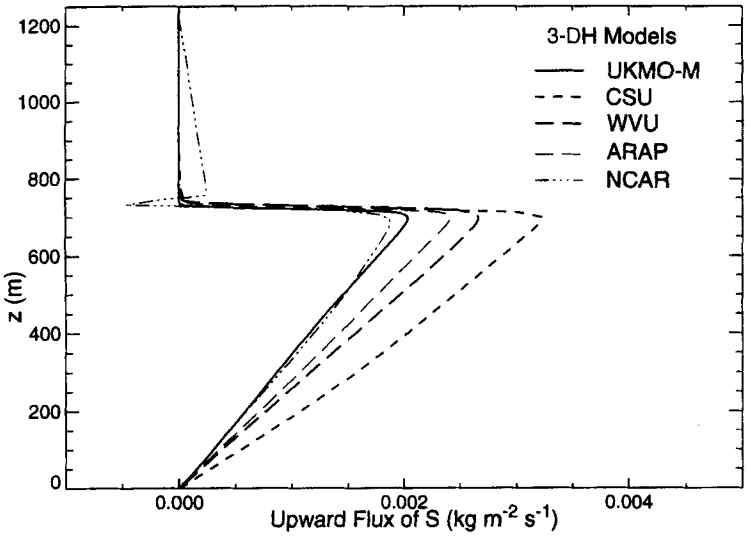

Figure 10. Vertical smoke-flux profile averaged over 2–3 h for 3-DH models.

this behaviour. The non-monotone NCAR model, however, exhibited negative fluxes at the inversion, with small positive values above that. Some curvature in the flux profiles within the boundary layer was exhibited by NCAR and CSU, indicating more statistical unsteadiness in the evolution of the upper boundary-layer. In addition, the flux at the inversion base in the non-monotone NCAR model is less than 70% of the mixed-layer prediction based on the 2–3 h w_e, suggesting a possible problem with patches to prevent negative smoke-concentrations. The profiles from 3-DM, 2-D and 1-D are not shown but were qualitatively similar to those from 3-DH. The magnitude of the flux maximum at the inversion was larger in 3-DM than in 3-DH, consistent with the higher values of w_e in

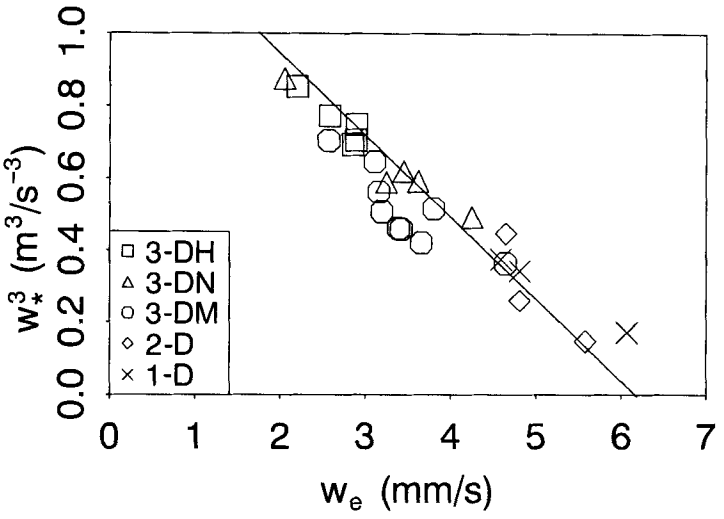

Figure 11. Variation of w_*^3 with w_e for all models. The line is the prediction of (11).

the 3-DM group. In 2-D and 1-D it was bigger still, typically twice the size of 3-DH. The smoke fluxes in 3-DN were negative at the inversion (cf. NCAR in 3-DH). The behaviour at levels above the inversion was determined by the details of the different patches applied to deal with undershoots and overshoots. Over the whole depth, there was a high degree of scatter between the different 3-DN runs.

(*e*) *Scaling of eddy velocity with convective velocity* w_*

Since there is no mean flow, the buoyancy fluxes drive the turbulence. Vertically integrated over the boundary layer, the source of $\mathrm{TKE_{blav}}$ resulting from the buoyancy fluxes is the vertical integral of the buoyancy flux, which is proportional to w_*^3. In this subsection, we compare w_* between models and check if different models produce the same relationship between measures of the strength of convection (such as $\mathrm{TKE_{blav}}$) and the driving of convection, as measured by w_*.

We saw in the previous subsection that, in a mixed-layer model, the convective heat flux is linearly related to w_e at all levels. Hence, w_*^3 is also linearly related to w_e, as we see by normalizing (9) into an expression for buoyancy flux as a function of z and integrating this over the boundary-layer depth:

$$w_*^3 = 1.25\frac{g}{\theta_0} z_i \frac{F_0}{\rho_0 C_p}\left(1 - \frac{2}{K_a \rho_0 z_i}\right) - 1.25 z_i w_e \Delta b. \tag{11}$$

Figure 11 shows how w_*^3 varies with w_e for all models. Most models are close to the theoretically expected line. Several 3-DM models lie somewhat below the line for reasons we do not yet understand.

Next, we test how well w_* correlates with direct measures of the strength of convection. One test, shown in Fig. 12, is to compare $\mathrm{TKE_{blav}}$ with w_*. The line $\sqrt{\mathrm{TKE_{blav}}} = 0.78 w_*$ is a least-squares fit (constrained to have zero intercept) of the $\mathrm{TKE_{blav}}$ from the 3-DH models to w_*. The 3-D models and the 1-D models lie close to this line. The 2-D models all scatter well to the right of the line, reflecting a different scaling $\sqrt{\mathrm{TKE_{blav}}} \approx 1.25 w_*$ for two-dimensional convection.

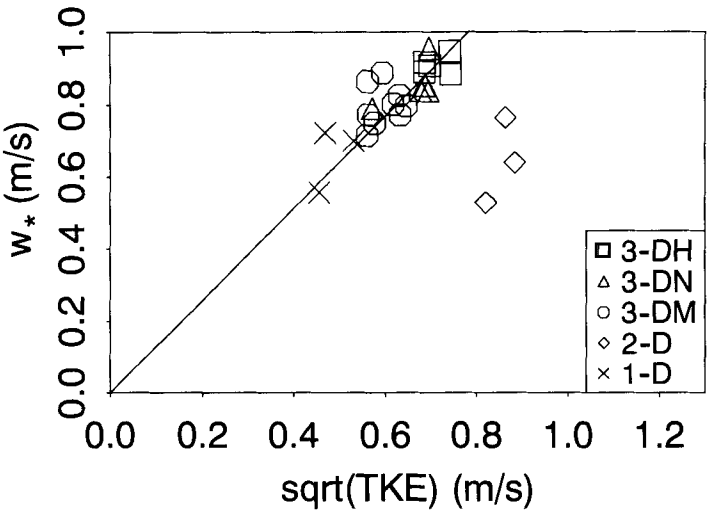

Figure 12. Variation of w_* with $\sqrt{\overline{\text{TKE}_{\text{blav}}}}$. Best-fit line is derived from the 3-DH models.

(*f*) *The empirical constant A*

Earlier, we showed that the model entrainment rates were higher than the range $0.2 \leqslant A \leqslant 0.4$ suggested by the laboratory experiments. In this subsection we make this comparison again, in a non-dimensional way, by computing the 2–3 h average entrainment efficiency A for each model. To do this, we use the calculated 2–3 h average w_e, convective velocity w_*, inversion strength Δb and z_i for that model. The relative variations between models in Δb (0.239–0.260 m s^{-2}) and z_i (710–750 m) are small, as these inversion parameters have drifted only slightly from their initial values during the three hours of simulation. Furthermore, w_* depends mainly on w_e. Thus, this comparison, shown in Fig. 13, can generally be regarded as a non-dimensional version of our earlier intercomparison of values of w_e.

All models have higher values of A than the range suggested by the laboratory experiments. The 3-DH models have the smallest values: 0.7 ± 0.1. The 3-DN models tend to have slightly lower values (1.0 ± 0.4) than the 3-DM models (1.3 ± 0.4), indicating the impact of the advection algorithm on entrainment efficiency if entrainment is not well resolved. Both are considerably larger than 3-DH, indicating the impact of vertical resolution. The 2-D and 1-D models have much larger entrainment efficiency (4 ± 2).

It is interesting to compare entrainment efficiency in simulations of the smoke cloud and of stratocumulus clouds, to see if LES models can reproduce the large disparity in A between dry and cloudy boundary-layers found by Nicholls and Turton (1986). Results from the earlier GCSS nocturnal-stratocumulus intercomparison were not archived for all models, but were available for the UKMO model with the standard and high vertical resolution used for the smoke-cloud simulations. The values of A computed for the stratocumulus simulation were 2.9 (cf. 1.01 for the smoke cloud) for standard vertical resolution and 2.2 (cf. 0.47 for the smoke cloud) for high vertical resolution. Thus, although the values of A for the modelled smoke-cloud may be overestimates, the UKMO model does indicate a large enhancement of A in stratocumulus. This suggests that LES models may be useful for understanding this enhancement. They are being studied in this context by several intercomparison participants.

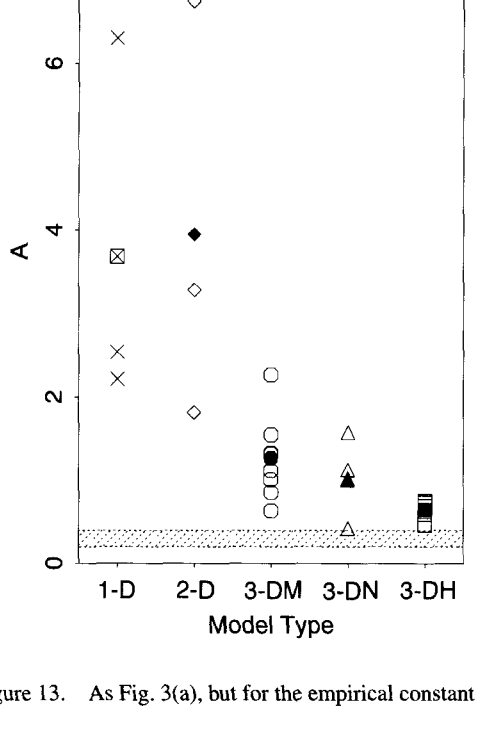

Figure 13. As Fig. 3(a), but for the empirical constant A.

(*g*) *Vertical profiles of velocity variances and TKE*

Many of the differences between models discussed so far are directly associated with model differences in advection schemes, coupled with inadequate resolution of the inversion. Within the convecting layer, the dominant eddies are well resolved by all 2-D and 3-D models. How similar is their statistical character between models? How does their vertical structure compare to eddies in surface-heated and cloud-topped boundary-layers? In this section, we consider the vertical profiles of vertical and horizontal velocity-variance, the TKE budget, and the profile of vertical-velocity skewness.

Figures 14 and 15 show the 2–3 h average vertical velocity and horizontal variances, $\overline{w'^2}$ and $\overline{u'^2} + \overline{v'^2}$, respectively, for the 3-DH models. All models closely agree in the boundary layer, with $\overline{w'^2}$ being symmetric about a maximum in the middle of the boundary layer despite the asymmetric forcing, and maxima in $\overline{u'^2} + \overline{v'^2}$ at the surface and the inversion. NCAR, which is the only 3-DH model that uses non-monotone advection, also has a similar, weaker variance-profile in the above-inversion layer associated with spurious weak convection.

Figures 16 and 17 show $\overline{w'^2}$ and $\overline{u'^2} + \overline{v'^2}$ for the UKMO 3-DH, 3-DM, 3-DN and 2-D models. These profiles are representative of differences between the model groups. In the boundary layer, the 3-DM and 3-DN models have profiles of $\overline{w'^2}$ and $\overline{u'^2} + \overline{v'^2}$ which are similar in shape to those of the 3-DH models, except that $\overline{w'^2}$ has slightly lower amplitude and the peaks in $\overline{u'^2} + \overline{v'^2}$ are somewhat less pronounced and sharp. The good agreement between the variance-profile shapes for the various types of 3-D model suggests that even the standard-resolution 3-D models are accurately simulating the large-eddy dynamics in the boundary layer below the inversion. Above the boundary layer, all the 3-DN models

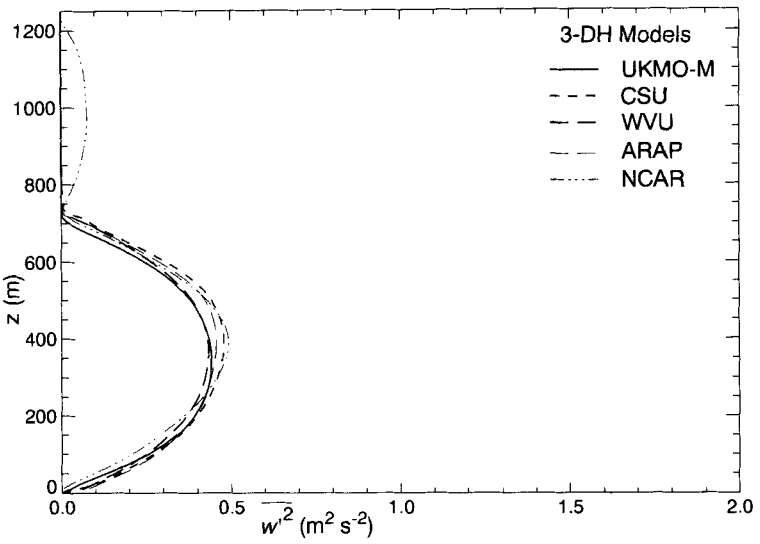

Figure 14. 2–3 h average vertical-velocity variance for the 3-DH models.

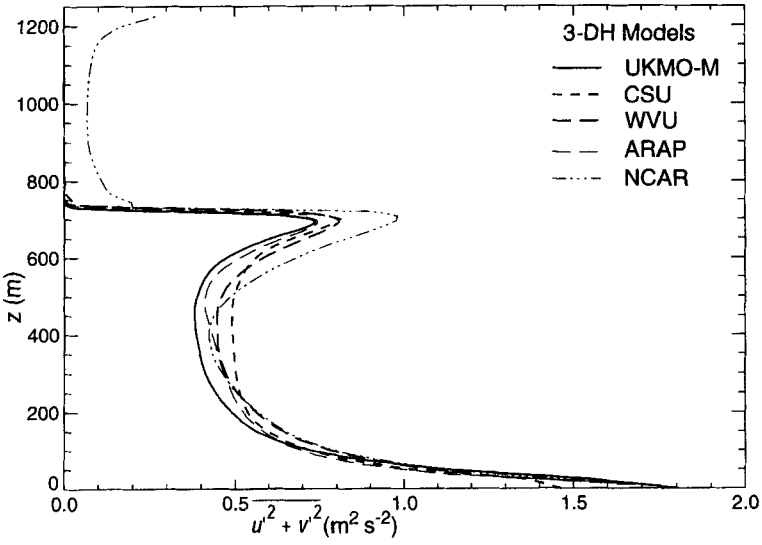

Figure 15. 2–3 h average horizontal-velocity variance for the 3-DH models.

have varying intensities of spurious convection, creating $\overline{w'^2}$ and $\overline{u'^2} + \overline{v'^2}$ profiles similar to the NCAR 3-DH model there.

The 2-D models have considerably different variance-profiles. They produce much larger $\overline{w'^2}$ with a somewhat narrower peak lower in the boundary layer, and broader peaks in $\overline{u'^2} + \overline{v'^2}$ at the inversion and the ground. There is more variability between models, but this may reflect temporal fluctuations in the TKE and heat flux (which are larger for the 2-D models) rather than fundamental differences between models.

The vertical and horizontal variances can be averaged to get the TKE profile, which is also calculated by the 1-D models. Figure 18 shows the TKE profiles for the UKMO

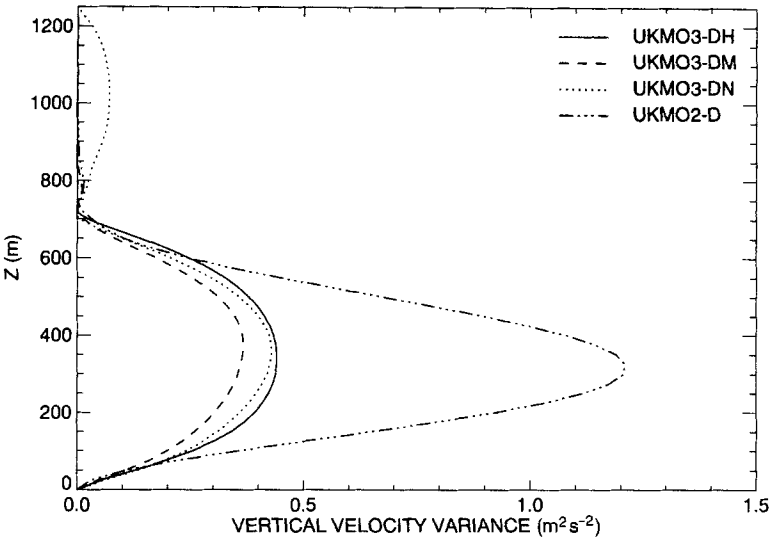

Figure 16. 2–3 h average vertical-velocity variance for the UKMO 3-D high-resolution, monotonic, non-monotonic and 2-D monotonic models.

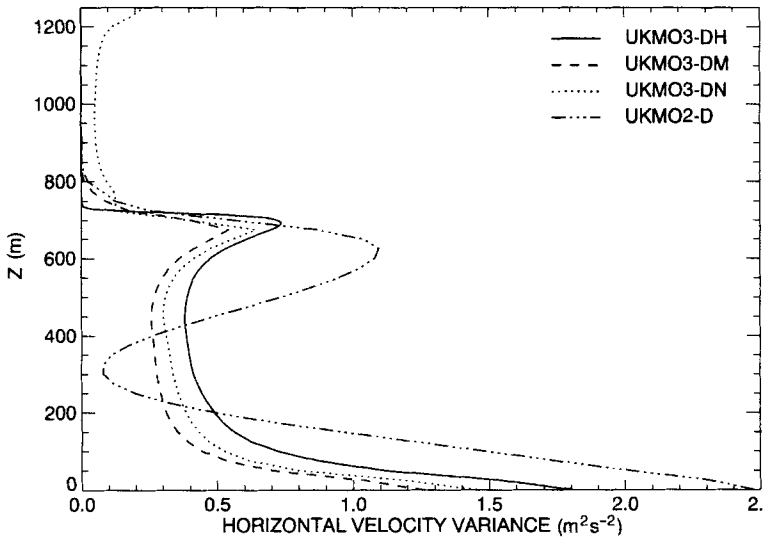

Figure 17. 2–3 h average horizontal-velocity variance for the UKMO 3-D high-resolution, monotonic, non-monotonic and 2-D monotonic models.

models and the AERO-HI model, which is representative of the 1-D models. The average magnitude of the TKE in the boundary layer varies considerably between model groups, as pointed out earlier. However, for all groups, TKE is fairly uniform with height throughout the boundary-layer depth except for larger values near the ground. By modifying the formulation of the turbulence lengthscale in the 1-D model shown, its TKE profile could probably be brought into excellent agreement with the 3-DH models.

The smoke cloud appears to have turbulence statistics which are intermediate between those of a surface-heated convective boundary-layer (e.g. LES simulations of Mason (1989)) and the nocturnal stratocumulus-capped boundary-layer studied in the first

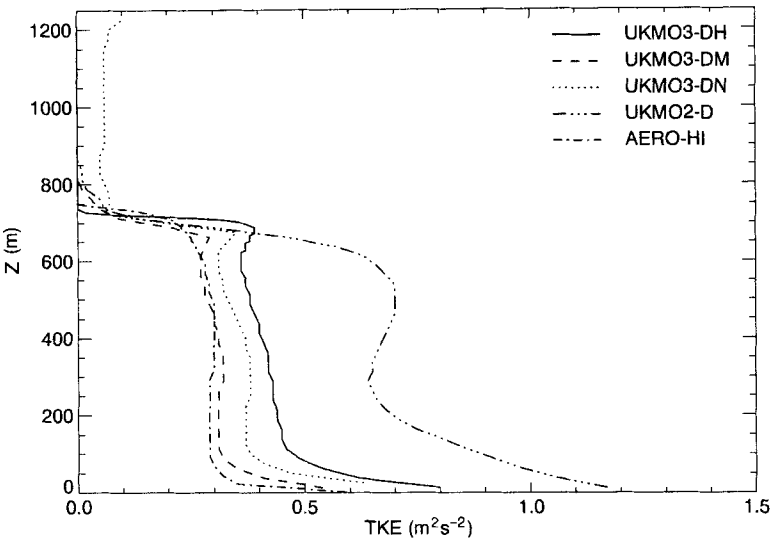

Figure 18. 2–3 h average TKE profile for the UKMO 3-D high-resolution, monotonic, non-monotonic and 2-D monotonic models, and the AERO-HI 1-D model.

intercomparison (Moeng *et al.* 1996). The surface-heated boundary-layer has its maximum value of $\overline{w'^2}$ at a height of $0.3z_i$, and so occurs lower in the boundary layer than in the smoke cloud. The profile $\overline{u'^2} + \overline{v'^2}$ in the surface-heated boundary-layer has a shape similar to that in the smoke cloud, but has a broader peak below the inversion. The TKE is twice as large in the lower half of the surface-heated boundary-layer as toward its top, as a result of the large buoyancy-fluxes near the surface. This concentration of TKE away from the entrainment interface may explain why the entrainment efficiency A for the smoke cloud (viz. 0.4) appears to be twice that for the surface-heated boundary-layer (0.2).

In the stratocumulus-capped boundary-layer, buoyancy fluxes are even more concentrated in the upper part of the boundary layer than in the smoke cloud. They are large mainly within the cloud that occupies the upper quarter of the boundary layer. Consequently, the TKE is 2–3 times as large just below the inversion as it is in the lower half of the boundary layer. The maximum of $\overline{w'^2}$ is within the cloud layer, and the peak of $\overline{u'^2} + \overline{v'^2}$ at the inversion is very pronounced. The concentration of TKE near the entrainment zone may contribute to the much larger entrainment rates in stratocumulus-capped boundary-layers than in a smoke cloud with the same Ri and w_*.

Figure 19 shows the 2–3 h average TKE budget for the UKMO high-resolution model. The buoyancy-flux profile (proportional to the vertical heat-flux) is the only source of boundary-layer averaged TKE. Shear generation of TKE is negligible, and storage is small. The dissipation of TKE is almost uniform with height, reflecting the uniformity of the TKE profile itself. Transport of TKE away from the regions of highest TKE generation in the upper part of the smoke layer into the inversion, and into the lower part of the smoke layer, balances the budget. In this model, the finite-difference algorithm used to integrate the model has been designed to allow a discrete formulation of the TKE budget with no budget residual. However, this is quite awkward to do, and no other model in the intercomparison conserves TKE discretely. While the budget residuals of most 3-DM and 3-DN models are small in the bulk of the boundary layer, they are typically as large as the other terms in the entrainment zone at the inversion for the standard-vertical-resolution

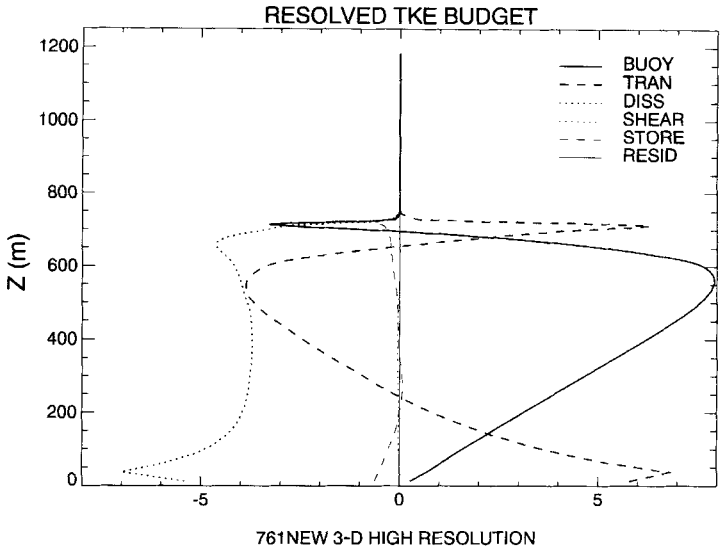

Figure 19. 2–3 h average TKE budget for the UKMO 3-D high-resolution model.

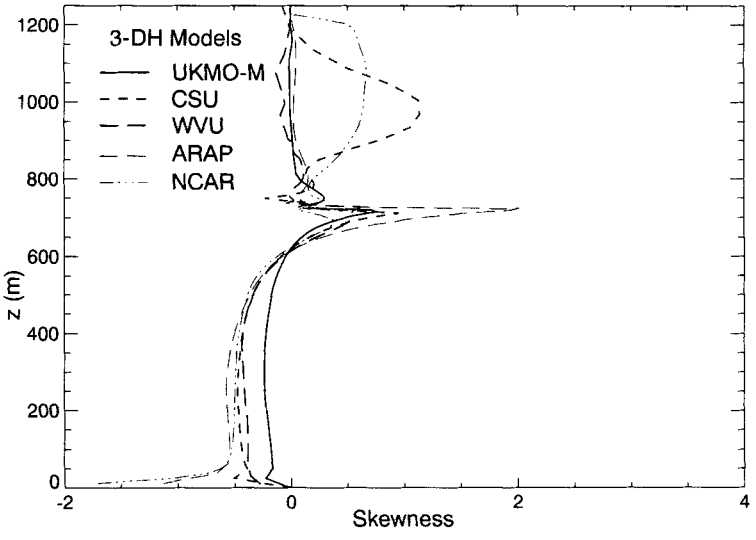

Figure 20. Vertical-velocity skewness for the 3-DH models.

models. The 3-DH models had smaller residuals at the inversion (of the order of 10% of the maximum buoyancy-flux in the smoke layer).

The vertical-velocity skewness $\overline{w'^3}/\overline{w'^2}^{3/2}$ for the 3-DH models is presented in Fig. 20. We will not comment on the behaviour in the region above the inversion, where the vertical-velocity variance is generally very small. All the 3-DH runs show a positive skewness at the inversion (updraughts more concentrated than downdraughts), as in Fig. 4, although with a large scatter in magnitude. Below the inversion, the skewness decreases, passing

through zero at the base of the radiative cooling zone (just above 600 m) and remaining almost constant from about 400 m to just above the surface. The skewness in the lower 400 m is typically −0.5 but only half that size in UKMO. This discrepancy is also observed at standard resolution and is not understood. The profiles from 3-DM (not shown) are both qualitatively and quantitatively similar to the monotone 3-DH models in Fig. 20. In the 3-DN models (not shown), as in the NCAR 3-DH profile, the positive skewness at the inversion is rather small (less than 0.5), with the exception of MNH. We conclude that the skewness profile is not highly sensitive to vertical resolution, but does appear to depend somewhat on the model and the type of advection scheme used. As one might expect, the differences in skewness profile between models are greatest near the inversion.

Only one of the 2-D runs (UW, not shown) exhibits negative skewness in the lower boundary-layer; in the others, it was generally positive but small. Near the inversion, the skewness in 2-D is typically positive and a little larger, but with a considerable scatter between models.

The 3-DH skewness-profiles are quite similar to those in nocturnal stratocumulus-capped boundary-layers, and very different from those in surface-heated boundary layers. Both observations and 3-D LES simulations of surface-heated boundary-layers show positive skewness at all heights (Moeng and Rotunno 1990), with values of 0.5–1 in the lower boundary layer. LES simulations suggest increased skewness in the upper quarter of the boundary layer, but this has not been seen in observations. LES skewness profiles in nocturnal stratocumulus from the first GCSS intercomparison were compiled but not published. While there was considerable scatter between the four LES simulations, the skewness profiles did tend to be similar to the smoke cloud case, with a narrow layer of positive skewness at the boundary layer top. Moeng and Rotunno (1990) obtained similar skewness-profiles for a similar case. Observations of skewness in marine stratocumulus generally agree with the LES-predicted profiles, although they suggest that the skewness at the inversion may be smaller than LES predictions, or even negative. Moyer and Young (1991) presented observations from one instance of nocturnal stratocumulus. It showed weakly positive skewness just below the inversion and negative skewness, down to −0.5, in the rest of the boundary layer. Aircraft observations of Nicholls and Leighton (1986) and tethered-balloon observations of Caughey *et al.* (1982) show downdraughts becoming increasingly spiky (i.e. increasingly negatively skewed) further below cloud-top.

5. Conclusions

The GCSS smoke-cloud intercomparison shows more definitively than previous studies that for accurately simulating cloud-topped boundary-layers under strong inversions, LES models must be run with higher vertical resolution in the inversion than is customary at present. We have hypothesized that, to calculate entrainment rate accurately, the vertical grid-spacing must be sufficiently small to resolve the horizontal variability of inversion height and thickness. For smoke clouds, and for many stratocumulus layers, this variability is as little as 5 m, though it may be much larger for weaker inversions, stronger convection, or if there is vertical wind-shear in the inversion. It is also necessary to resolve the vertical profile of radiative cooling at the smoke-cloud top accurately. In the GCSS intercomparison and real stratocumulus clouds, this may also require 10 m or smaller vertical grid-spacing; further systematic study of this issue is required.

Models with vertical grid-spacing of 5–12.5 m in the inversion predict entrainment rates 10–50% larger than predictions extrapolated from laboratory experiments. With customary vertical grid-spacing of 25 m or more, 1-D, 2-D and 3-D models all tend (with some scatter) to predict entrainment rates significantly higher than the high-vertical-resolution

3-D models. The participating 1-D models also tend to underestimate TKE, but perform reasonably well, given their simplicity. 2-D models produce too much entrainment and considerably overestimate TKE, as compared with 3-D models with the same numerical formulation. For 3-D models, the entrainment rate appears to be sensitive mainly to the vertical grid-spacing within the layer around the inversion; away from this region, a 25 m vertical grid-spacing appears adequate.

For 3-D models, different types of advection algorithm tend to produce different entrainment rates for smoke clouds. Compared to the predictions of laboratory experiments, monotone advection-schemes with 25 m vertical grid-spacing overestimate entrainment rate slightly more than non-monotone schemes, but are less likely to produce some other problems, such as negative smoke-concentrations in the upper layer, spurious positive smoke-concentrations in the upper layer large enough to have a noticeable radiative feedback, and spurious buoyancy-fluxes as a result of temperature overshoots at the top of the inversion. There were also some model differences in statistical features of the large eddies (in particular skewness) that may reflect the type of advection scheme. The subgrid-scale formulation may also contribute to differences in the entrainment rate between models (particularly for the MNH 3-DN model). However, a 3-D monotone-advection model run without any subgrid-scale scheme, gave results comparable to those from other models of this group.

Should we disregard most published LES simulations of stratocumulus layers on account of problems of under-resolution? This would be too extreme a conclusion to draw from the present paper. Many internal features of the turbulent profiles, such as the vertical profiles of velocity variances, are adequately represented in the smoke-cloud case by 3-D models even when the entrainment is too efficient. In long-term integrations, the excessively efficient entrainment will not necessarily over-deepen the evolving boundary layer dramatically. Instead, energy-balance arguments (Bretherton and Wyant 1997) suggest that the internal turbulent structure of the boundary layer adjusts over periods of a few hours to be consistent with a nearly model-independent entrainment rate, with comparatively small model-differences in the vertical thermodynamic profiles. In this way, under-resolved 3-D and even 2-D and 1-D models can still be useful guides to boundary-layer evolution as long as it is not also necessary to predict turbulence levels within the boundary layer accurately.

The smoke-cloud intercomparison is a natural starting point for a variety of investigations, some of which are now in progress. Several issues concerning resolution were brought up in this intercomparison but were not fully addressed. Firstly, is fine horizontal resolution in the entrainment interface also necessary? Even in the high-vertical-resolution simulations, there is no indication of overturning small eddies at the entrainment interface; the 50 m horizontal grid-spacing used in all models would not resolve such eddies if they existed. This suggests that finer horizontal resolution might change the modelled structure of the entrainment interface qualitatively. Stevens and Bretherton (1999) found that if both the horizontal and vertical grid-spacings are small, the entrainment rate is somewhat larger than if only the vertical grid-spacing is small. On the other hand, at the GCSS workshop, D. Lewellen presented a series of simulations with vertical grid-spacing 5 m and horizontal grid-spacings *larger* than the standard values that showed the entrainment rate to be insensitive to horizontal grid-spacing.

A second topic is an indirect feedback of resolution on entrainment. Many authors writing about mixed-layer modelling point out that radiation from air in the inversion reduces the strength of the inversion, whereas from air beneath the inversion radiation stimulates convection, with different effects on entrainment. Grid resolution affects the spatial distribution of smoke, and hence cooling, near the inversion. Some participants have begun to look at how this may feed back on entrainment rate by changing the specification

of the radiative forcing. For instance, one can change the absorptivity of the smoke, or by analogy to a real cloud, impose a threshold smoke-concentration below which no cooling occurs.

A third topic for further study is the entrainment scaling (1). For smoke clouds, we are lucky to have a laboratory analogue that supports this scaling. One of the chief attractions of using LES models on more idealized problems is that they allow us to extend the entrainment scaling to more realistic settings (stratocumulus clouds) by performing a series of simulations with systematic variations of parameters such as inversion strength, cloud liquid-water content, downwelling long-wave and short-wave radiation and so on. The utility of this approach relies on the accuracy of the LES-calculated entrainment-rate. In this study, we have not tried to use an LES to verify even the inverse-Richardson-number scaling relation (1). However, by using either higher resolution or by focusing on weaker inversions, reliable LES entrainment-rates to carry out such a study may be obtainable. Wide-ranging studies along these lines have been completed by Lock (1996) and Stevens and Bretherton (1999).

Acknowledgements

We thank Aad van Ulden and our participants from KNMI and IMAU for hosting the workshop that inspired this paper. Funding for this work was provided by many sources, including grants NASA NAG1-1711 (Bretherton, Rand, Wyant), European Commission contract ERBCHBGCT920232 (Cuxart) and ONR grant N00014-93-1-0395 (Lewellen).

Appendix

Acronyms and references for the model codes

UKMO	Meteorological Office, United Kingdom, LES (MacVean 1993)
UW	University of Washington, USA, LES (Wyant *et al.* 1997)
SB	Dave Stevens LES (Stevens and Bretherton 1996)
NCAR	National Center for Atmospheric Research, USA, LES (Moeng 1984; Moeng 1986)
CSU	Colorado State University, USA, LES (Stevens *et al.* 1996)
CU	University of Colorado, USA, LES (Moeng 1986; Kosovic 1996)
MNH	Meso-NH model (Cuxart *et al.* 1997)
MPI	Max-Planck-Institut für Meteorologie, Germany, LES (Chlond 1992; 1994)
IMAU	Institute for Marine and Atmospheric Research, Utrecht, The Netherlands, LES (Cuijpers and Duynkerke 1993)
WVU	West Virginia University, USA, LES (Lewellen *et al.* 1996)
ARAP	Titan Research and Technology, USA, LES (Sykes and Henn 1989)
UOK	University of Oklahoma, Co-operative Institute for Mesoscale Meteorological Studies, USA, LES (Kogan *et al.* 1995)
AERO	Observatoire Midi-Pyrénées, France, 1-D model (Bechtold *et al.* 1992)

References

Bechtold, P., Fravalo, C. and Pinty, J.-P. 1992 A model of marine boundary-layer cloudiness for mesoscale applications. *J. Atmos. Sci.*, **49,** 1723–1744

Bretherton, C. S. and Wyant, M. C. 1997 Moisture transport, lower tropospheric stability and decoupling of cloud-topped boundary-layers. *J. Atmos. Sci.*, **54,** 148–167

Bretherton, C. S., Austin, P. and Siems, S. T. 1995 Cloudiness and marine boundary-layer dynamics in the ASTEX Lagrangian experiments. Part II: Cloudiness, drizzle, surface fluxes and entrainment. *J. Atmos. Sci.*, **52,** 2724–2735

Caughey, S. J., Crease, B. A. and Roach, W. T. 1982 A field study of nocturnal stratocumulus: II. Turbulence structure and entrainment. *Q. J. R. Meteorol. Soc.*, **108,** 125–144

Chlond, A. 1992 Three-dimensional simulation of cloud-street development during a cold-air outbreak. *Boundary-Layer Meteorol.*, **58,** 161–200

1994 Locally-modified version of Bott's advection scheme. *Mon. Weather Rev.*, **122,** 111–125

Cuijpers, J. W. M. and Duynkerke, P. G. 1993 Large-eddy simulation of trade-wind cumulus clouds. *J. Atmos. Sci.*, **50,** 3894–3908

Cuxart, J. 1997 *Planetary boundary-layer simulation: From LES to general circulation models*. Ph.D. Thesis, Universitad de Barcelona

Deardorff, J. W. 1980 Cloud-top entrainment instability. *J. Atmos. Sci.*, **37,** 131–147

Del Genio, A. D., Yao, M.-S., Kovari, W. and Lo, K. K.-W. 1996 A prognostic cloud-water parameterization for global climate models. *J. Climate*, **9,** 270–304

De Roode, S. R. and Duynkerke, P. G. 1997 Observed Lagrangian transition of stratocumulus into cumulus during ASTEX: Mean state and turbulence structure. *J. Atmos. Sci.*, **54,** 2157–2173

E, X. and Hopfinger, E. J. 1986 On mixing across an interface in stably stratified fluid. *J. Fluid Mech.*, **166,** 227–244

Fernando, H. J. S. 1991 Turbulent mixing in stratified fluids. *Ann. Rev. Fluid Mech.*, **23,** 455–493

GEWEX Cloud System Science Team 1993 The GEWEX Cloud System Study (GCSS) *Bull. Am. Meteorol. Soc.*, **74,** 387–399

Kato, H. and Phillips, O. M. 1969 On the penetration of the turbulent layer into a stratified fluid. *J. Fluid Mech.*, **37,** 643–665

Kawa, S. R. and Pearson, Jr., R. 1989 An observational study of stratocumulus entrainment and thermodynamics. *J. Atmos. Sci.*, **46,** 2649–2661

Kogan, Y. L., Khairoutdinov, M. P., Lilly, D. K., Kogan, Z. N. and Liu, Q. 1995 Modeling of stratocumulus cloud layers in a large eddy simulation model with explicit microphysics. *J. Atmos. Sci.*, **52,** 2923–2940

Kosovic, B. 1997 Subgrid-scale modelling for the large-eddy simulation of high Reynolds number boundary layers. *J. Fluid Mech.*, **336,** 151–182

Lewellen, D. C., Lewellen, W. S. and Yoh, S. 1996 Influence of Bowen ratio on boundary-layer cloud structure. *J. Atmos. Sci.*, **53,** 175–187

Lilly, D. K. 1967 'The representation of small-scale turbulence in numerical simulation experiments.' Pp. 195–210 in proceedings of IBM scientific computing symposium on environmental science, Yorktown Height, NY, USA

1968 Models of cloud-topped mixed layers under a strong inversion. *Q. J. R. Meteorol. Soc.*, **94,** 292–309

Lock, A. P. 1996 *Entrainment in clear and cloudy boundary-layers*. Ph.D thesis, University of Manchester Institute of Science and Technology

MacVean, M. K. 1993 A numerical investigation of the criterion for cloud-top entrainment instability. *J. Atmos. Sci.*, **50,** 2481–2495

Mason, P. J. 1989 Large-eddy simulation of the convective boundary layer. *J. Atmos. Sci.*, **46,** 1492–1516

McEwan, A. D. and Paltridge, G. W. 1976 Radiatively driven thermal convection bounded by an inversion—a laboratory simulation of stratus clouds. *J. Geophys. Res.*, **81,** 1095–1102

Moeng, C.-H. 1984 A large-eddy simulation model for the study of boundary layer turbulence. *J. Atmos. Sci.*, **41,** 2052–2062

1986 Large-eddy simulation of a stratus-topped boundary layer. Part 1: Structure and budgets. *J. Atmos. Sci.*, **43,** 2886–2900

Moeng, C.-H. and Rotunno, R. 1990 Vertical velocity skewness in the buoyancy-driven boundary layer. *J. Atmos. Sci.*, **47,** 1149–1162

Moeng, C.-H., Cotton, W. R., Bretherton, C. S., Chlond, A., Khairoutdinov, M., Krueger, S., Lewellen, W. S., MacVean, M. K., Pasquier, J. R. M., Rand, H. A., Siebesma, A. P., Sykes, R. I. and Stevens, B. 1996 Simulation of a stratocumulus-topped PBL: Intercomparison among different numerical codes. *Bull. Am. Meteorol. Soc.*, **77,** 261–278

Moyer, K. and Young, G. 1991 Observations of vertical velocity skewness within the marine-topped boundary layer. *J. Atmos. Sci.*, **48,** 403–410

Nicholls, S. and Leighton, J. 1986 An observational study of the structure of stratiform cloud sheets: Part I. Structure. *Q. J. R. Meteorol. Soc.*, **112,** 431–460

Nicholls, S. and Turton, J. D. 1986 An observational study of the structure of stratiform cloud layers: Part II. Entrainment. *Q. J. R. Meteorol. Soc.*, **112,** 461–480

Nieuwstadt, F. T. M. and Businger, J. A. 1984 Radiative cooling near the top of a cloudy mixed layer. *Q. J. R. Meteorol. Soc.*, **110,** 1073–1078

Nieuwstadt, F. T. M., Mason, P. J., Moeng, C.-H. and Schumann, U. 1992 Large-eddy simulation of the convective boundary layer: A comparison of four computer codes. Pp. 343–367 in *Turbulent Shear Flows, Vol. 8*, F. Durst, Ed., Springer-Verlag

Randall, D. A., Abeles, J. A. and Corsetti, T. G. 1985 Seasonal simulations of the planetary boundary layer and boundary-layer stratocumulus with a general circulation model. *J. Atmos. Sci.*, **42,** 641–676

Sayler, B. and Breidenthal, R. E. 1997 Laboratory simulations of radiatively induced entrainment in stratiform clouds. *J. Geophys. Res.*, **103,** 8827–8837

Shy, S. and Breidenthal, R. E. 1991 Turbulent stratified interfaces. *Phys. Fluids A*, **3,** 1278–1285

Smagorinsky, J. 1963 General circulation experiments with the primitive equations. I. The basic experiment. *Mon. Weather Rev.*, **91,** 99–164

Smolarkiewicz, P. K. and Clark, T. L. 1986 The multidimensional positive definite advection transport algorithm: Further developments and applications. *J. Comput. Phys.*, **67,** 396–438

Stephens, G. L. 1978 Radiative properties of extended water clouds. Parts I and II. *J. Atmos. Sci.*, **35,** 2111–2132

Stevens, D. E. and Bretherton, C. S. 1996 A forward-in-time advection scheme and adaptive multi-level flow solver for nearly incompressible atmospheric flow. *J. Comput. Phys.*, **129,** 284–295

1999 Effects of resolution on the simulation of stratocumulus entrainment. *Q. J. R. Meteorol. Soc.*, **125,** 425–439

Stevens, B., Walko, R. L., Cotton, W. R. and Feingold, G. 1996 Elements of the microphysical structure of numerically simulated nonprecipitating stratocumulus. *J. Atmos. Sci.*, **53,** 980–1007

Stull, R. B. 1976 The energetics of entrainment across a density interface. *J. Atmos. Sci.*, **33,** 1260–1267

Sykes, R. I. and Henn, D. S. 1989 Large-eddy simulation of turbulent sheared convection. *J. Atmos. Sci.*, **46,** 1106–1118

Tennekes, H. 1973 A model for the dynamics of the inversion above a convective boundary layer. *J. Atmos. Sci.*, **30,** 558–567

Turner, J. S. 1968 The influence of molecular diffusivity on turbulent entrainment across a density interface. *J. Fluid Mech.*, **33,** 639–656

1973 *Buoyancy effects in fluids*. Cambridge University Press

Wyant, M. C., Bretherton, C. S., Rand, H. A. and Stevens, D. E. 1997 Numerical simulation and a conceptual model of the stratocumulus to trade cumulus transition. *J. Atmos. Sci.*, **54,** 168–192